Title
Structure of the μ-opioid receptor–Gi protein complex

Journal
Nature, 558(7711)

ISSN
0028-0836

Authors
Koehl, Antoine
Hu, Hongli
Maeda, Shoji
et al.

Publication Date
2018-06-01

DOI
10.1038/s41586-018-0219-7

Peer reviewed

Published in final edited form as:

Nature. 2018 June ; 558(7711): 547–552. doi:10.1038/s41586-018-0219-7.

Structure of the μ Opioid Receptor-G_i Protein Complex

Antoine Koehl[1,*], **Hongli Hu**[1,2,*], **Shoji Maeda**[2,*], **Yan Zhang**[1,2], **Qianhui Qu**[1,2], **Joseph M. Paggi**[1,2,7,8], **Naomi R. Latorraca**[1,2,7,8,9], **Daniel Hilger**[2], **Roger Dawson**[3], **Hugues Matile**[3], **Gebhard F. X. Schertler**[10,11], **Sebastien Granier**[4], **William I. Weis**[1,2], **Ron O. Dror**[1,2,7,8,9], **Aashish Manglik**[5,6,†], **Georgios Skiniotis**[1,2,†], and **Brian K. Kobilka**[2,†]

[1]Department of Structural Biology, Stanford University School of Medicine, 279 Campus Drive, Stanford, California 94305, USA [2]Department of Molecular and Cellular Physiology, Stanford University School of Medicine, 279 Campus Drive, Stanford, California 94305, USA [3]Roche Pharma Research and Early Development, Therapeutic Modalities, Roche Innovation Center Basel, F.Hoffmann-La Roche Ltd, Grenzacherstrasse 124, 4070 Basel, Switzerland [4]Institut de Génomique Fonctionnelle, INSERM [5]Department of Pharmaceutical Chemistry, University of California San Francisco, 1700 4th Street, San Francisco, California 94143, USA [6]Department of Anesthesia and Perioperative Care, University of California San Francisco, 1700 4th Street, San Francisco, California 94143, USA [7]Department of Computer Science, Stanford University, Stanford, CA 94305, USA [8]Institute for Computational and Mathematical Engineering, Stanford University, Stanford, CA 94305, USA [9]Biophysics Program, Stanford University, Stanford, CA 94305, USA [10]Laboratory of Biomolecular Research, Paul Scherrer Institute, 5232 Villigen PSI, Switzerland [11]Department of Biology, ETH Zürich, Wolfgang-Pauli-Strasse 27, 8093 Zürich, Switzerland

Abstract

Correspondence and requests for materials should be addressed to A.M. (Aashish.Manglik@ucsf.edu), Georgios Skiniotis (yiorgo@stanford.edu), or Brian Kobilka (kobilka@stanford.edu).

*Authors contributed equally to this work

†Co-corresponding

Author Contributions

A.K. prepared the μOR-G_i complex and refined the structure from cryo-EM density maps. H.H. obtained and processed cryo-EM data with the assistance of Y.Z. and Q.Q. S.M. identified and prepared scFv16 with assistance from R.D. and H.M and under supervision of G.F.X.S. A.M., D.H. S.G. and A.K. developed the procedure for forming the μOR-G_i complex. N.R.L and J.M.P performed molecular dynamics simulations under supervision of R.O.D. W.I.W. aided in map interpretation and model refinement. A.K., A.M. B.K.K. and G.S. wrote the manuscript. A.M., G.S. and B.K.K. supervised the project.

Author Information

The authors declare one competing interest: Brian Kobilka is a founder of and consultant for ConfometRx, Inc. Readers are welcome to comment on the online version of the paper.

Data availability

All data generated or analyzed during this study are included in this published article and its Supplementary Information. Sequences of constructs used in this study are listed in Supplementary Figure 1. The cryo-EM density maps for the μOR-G_i complex with, and without, scFv16 have been deposited in the Electron Microscopy Data Bank under accession codes EMD-XXXX and EMD-YYYY, respectively. The coordinates for the models of μOR-G_i with, and without scFv-16 have been deposited in the Protein Data Bank under accession numbers XXXX and YYYY respectively.

The μ opioid receptor (μOR) is a G protein-coupled receptor (GPCR) that is the target of most clinically and recreationally used opioids. The induced positive effects of analgesia and euphoria are mediated by μOR signaling through the adenylyl cyclase-inhibiting heterotrimeric G protein G_i. We present the 3.5-Å resolution cryo-electron microscopy (cryo-EM) structure of the μOR bound to the agonist peptide DAMGO and nucleotide-free G_i. DAMGO occupies the morphinan ligand pocket, with its N-terminus interacting with conserved receptor residues while its C-terminus engages regions important for opioid ligand selectivity. Comparison of the μOR-G_i complex to previously determined structures of other GPCRs bound to the stimulatory G protein G_s reveals differences in the movement of transmembrane receptor helix 6 and in the interactions between the G protein α subunit and the receptor core. Together, these results shed light into the structural features that contribute to the G_i protein coupling specificity of the μOR.

The μOR is the primary target of morphine and many clinically used opioid analgesics[1]. Opioid binding to the μOR leads to clinically desired analgesic and antitussive actions but also important negative side effects including addiction and potentially lethal respiratory suppression. Opioids have become the most prescribed class of medication in the United States[2], leading to a national epidemic of addiction and an unprecedented level of drug overdose deaths.

Like other GPCRs, the μOR achieves many of its physiological actions by stimulating signaling via a heterotrimeric G protein. While other GPCRs have been shown to signal through more than one G protein subtype, the μOR signals almost exclusively through the adenylyl-cyclase inhibitory family of G proteins ($G_{i/o}$)[3]. The analgesic activity of opioids is driven by G protein activation[4], but activated μOR can also interact with β-arrestins, whose recruitment has been associated with the respiratory depression induced by many opioids[5,6]. Recently developed molecules that favor G_i signaling over arrestin recruitment display analgesic efficacy with reduced side effects, suggesting that different signaling pathways can be selectively targeted to yield unique physiological outcomes[7,8]. Though a framework for GPCR interactions with the stimulatory G protein G_s has recently been enabled by X-ray crystallography[9] and cryo-electron microscopy (cryo-EM)[10,11], the structural basis for GPCR signaling through other G protein subtypes remains undefined. To better understand the mechanism of selective activation of G_i by the μOR, we sought to determine the structure of the μOR-G_i complex.

3.5-Å cryo-EM map of a μOR-G_i complex

DAMGO (H-Tyr-D-Ala-Gly-*N*-MePhe-Gly-OH) is a μOR-selective synthetic analog of the natural peptide agonist enkephalin. DAMGO-bound μOR was incubated with G_{i1} heterotrimer and the complex was treated with the nucleotide hydrolase apyrase to remove GDP. The resulting nucleotide-free complex was further stabilized by a single-chain variable fragment (scFv16) that binds to heterotrimeric G_i (Extended Data Figure 1) and prevents GTPγS mediated dissociation of nucleotide-free complexes. We applied single-particle cryo-EM to initially obtain a three-dimensional map of the μOR-DAMGO-G_i-scFv16 complex at an indicated nominal resolution of 3.6 Å (Extended Data Fig. 2–3, Extended Data Table 1). Notably, scFv16 binds a composite interface comprised of the αN helix of

$G\alpha_i$ and the β propeller of Gβ, a site that is more than 20 Å distal to the μOR-$G\alpha_i$ interface and does not perturb the interface between Gα and Gβ subunits (Extended Data Figure 1). Subtraction of the scFv16 signal from raw particle images led to an improved map with an indicated global resolution of 3.5 Å. This map displayed enhanced features particularly in the receptor transmembrane core (Extended Data Figures 2, 3, 4), enabling the high resolution visualization of the μOR-G_i interface and ligand binding. Accordingly, we employed this improved 3.5-Å map to examine interactions between μOR and DAMGO, and between μOR and G_i (Fig. 1a, b).

Activation of μOR by a peptide agonist

We previously determined the active-state crystal structure of μOR bound to the morphinan agonist BU72 and an active-state stabilizing nanobody (Nb39) at a resolution of 2.2 Å[12]. Like other small molecule morphinans, BU72 is rigidified by a complex ring system, in contrast to flexible opioid peptides like DAMGO that have multiple rotatable bonds. The cryo-EM map includes well-defined features for most amino acids forming the orthosteric binding pocket (Extended Data Fig. 4a). Despite differences in agonist structure, the conformation of the active-state binding pocket and the orientation of the amino acids that interact with the agonist are highly similar for the μOR bound to BU72 or DAMGO (Fig. 1c), suggesting that the μOR recognizes structurally distinct agonists in a stereotypic manner.

Although DAMGO is a flexible ligand, we observe density for the entire peptide bound to the receptor (Fig. 1a, Extended Data Fig. 3, 4). The DAMGO N-terminus occupies a similar position in the binding pocket as BU72. In contrast, the C-terminus of DAMGO extends ~8 Å further towards the extracellular loops compared to BU72 (Fig. 1d, e). To identify stable atomic-level interactions between DAMGO and the binding pocket, we performed molecular (MD) dynamics simulations. In over 1μs of simulation, DAMGO remained close to its initially modeled pose, with the amino-terminal portion largely remaining confined to the experimentally determined EM density (Fig. 1f, Extended Data Fig 5). The DAMGO N-terminus maintained a persistent salt bridge with $D147^{3.32}$, a feature previously observed in structures of morphinans bound to opioid receptors (Fig. 1e; superscripts indicate Ballesteros-Weinstein numbering for GPCRs[13]). The same amine group also often formed a hydrogen bond with $Y326^{7.43}$. More generally, the amino-terminal Tyr of DAMGO overlaps the phenolic group of other small molecule opioids characterized previously by X-ray crystallography[14–17].

MD simulations also revealed a water-mediated hydrogen bonding network that closely overlaps with the water network observed in the high-resolution crystal structure of μOR[12] (Extended Data Fig. 6). In particular, the simulations revealed a stable, water-mediated interaction formed between the DAMGO phenol and $H297^{6.52}$. Though the crystal structure of the μOR bound to BU-72 shows two water molecules bridging the DAMGO phenol and $H297^{6.52}$, simulations of μOR bound to DAMGO and other phenolic ligands[8,12] suggest that one of these waters rapidly dissociates and that a single water is required for stable ligand binding. This interaction is a hallmark of opioid recognition that has been observed for

morphinans in complex with the μOR[12,14] as well as other small molecule and peptide-mimetic agonists for the homologous δ and κ opioid receptors (κOR)[15,16,18].

DAMGO is more than 500-fold selective for the μOR over the δOR and κOR[19]. As elucidated in prior structures, ligand interactions with the extracellular loops encode ligand subtype specificity among closely related opioid receptors[15]. Indeed, DAMGO selectivity for μOR over δOR has been shown to result from residues in ECL1 while selectivity over κOR results from differences in ECL3[20]. The map density for the carboxy-terminal residues of DAMGO is slightly weaker than for the amino-terminus, consistent with increased mobility of this region in simulations (Fig. 1f, Extended Data Fig 5). In our model, the DAMGO N-Me-Phe side chain occupies a conserved hydrophobic pocket near ECL1 and the Gly-OH group folds back over the ligand (Fig. 1e). This model is consistent with the high affinity μOR binding of cyclized enkephalins that bridge the +2 and +5 positions of the peptide[21].

Structure of G_i-Stabilized Active μOR

The overall structure of G_i-bound μOR is similar to the active conformation of the BU72-bound μOR stabilized by Nb39 (root mean square deviation of 1 Å)[12] with a predominant outward displacement of TM6 from the heptahelical bundle relative to the inactive state (Fig. 2a, b). A number of highly conserved residues in the GPCR family have been shown to be important for receptor activation, including the $D^{3.49}R^{3.50}Y^{3.51}$, the $N^{7.49}P^{7.50}xxY^{7.53}$, and conserved core triad ($I^{3.40}$, $P^{5.50}$, and $F^{6.44}$) motifs. The conformation of each of these regions in the μOR-G_i complex is virtually identical to the active state observed in complex with Nb39 (Fig. 2c). The structural similarity of μOR between Nb39 and G_i-coupled states indicate that these changes underlie ligand-mediated activation and are not specific to a particular intracellular binder. Indeed, Nb39 and G_i promote a similar increase in agonist affinity[12], which supports a common mechanism of allosteric communication between the intracellular G protein coupling domain and the ligand binding pocket[12].

Two differences between Nb39 and G_i stabilized active-states of μOR are particularly notable. First, compared with the nanobody-stabilized active-state μOR, TM6 in the μOR-G_i complex is further displaced by 3 Å towards TM7 (Fig. 2b). Second, the conformation of intracellular loop 3 (ICL3) is different in the two structures (Fig. 2a). It is likely that the specific ICL3 conformation of μOR stabilized by Nb39 reflects interactions that are unique to the nanobody rather than a general feature of receptor activation prior to G protein coupling. A similar difference in ICL3 conformation was previously observed for the β_2-adrenergic receptor (β_2AR) between nanobody (Nb80)[22] and G_s-coupled states. The comparison of the G protein bound states of both receptors shows that the β_2AR TM6 is displaced outward by another 9 Å compared to the μOR (Fig. 2d).

Structural Changes in G_i

The quality of the cryo-EM map enabled accurate modeling of G_i in its nucleotide-free state, providing insight into the structural changes that underlie nucleotide release. The changes we observe are similar to those observed in nucleotide-free G_s in complex with other

GPCRs. The most striking difference between the GDP bound[23] and nucleotide free heterotrimer in complex with μOR involves the separation of the α-helical domain (AHD) from the Ras-like domain in the alpha subunit of G_i ($G\alpha_i$) (Fig. 3a). Due to its relative flexibility, we excluded the AHD density from the high-resolution map refinement. The dynamic character of the AHD has been observed previously by spectroscopic and structural studies in complexes between receptors and both G_s[9–11] and G_i[24,25]. Displacement of the AHD disrupts several contacts with GDP and is necessary, but not sufficient for nucleotide release, a process that involves breaking additional contacts with the Ras domain[24].

G_i coupling to the μOR also involves a 6-Å translation as well as a 60° rotation of the $G\alpha_i$ α5 helix into the receptor core (Fig. 3b). This movement has been shown to be essential for nucleotide release in G_i[24]. In particular, the motion of α5 leads to a change in the position of the β6-α5 loop containing the conserved TCAT motif that forms direct interactions with the guanine base of GDP. This displacement disrupts key contacts between the G protein and nucleotide. Furthermore, the observed translation and rotation of the α5 helix requires the displacement of the fully conserved F336 away from the hydrophobic pocket formed by residues in the β2/β3 strands and the α1 helix[26] (Fig. 3b). Movement of the α5 helix is also propagated to the phosphate binding P-loop connecting the β1 strand and the α1 helix by disruption of a hydrophobic network between the α1 and α5 helices (Fig. 3b–d). Correspondingly, upon transition of G_i to the nucleotide-free state, we observe a 4-Å shift of α1 towards the α5 helix in G_i whereby the hydrophobic contacts are replaced by polar interactions with the β6-α5 loop as it is released from its guanine binding position (Fig. 3c, d). These changes contrast those observed in structures of G_s-coupled complexes, in which α1 not only becomes more unstructured, but also tends to lose interactions with the α5 helix (Fig. 3e). Our structure is consistent with previous studies suggesting that engagement of a GPCR with the α5 helix and αN- β1 loop leads to concerted changes in the α1 helix and P loop that destabilize contacts with the guanine nucleotide leading to its release[27].

Structural insights into G_i coupling specificity of the μOR

Although the μOR couples exclusively to $G_{i/o}$[3], many GPCRs can couple to multiple G protein subtypes; a well-studied example is the β_2AR, which couples to both G_s and $G_{i/o}$. Prior sequence-level analyses have failed to identify a linear GPCR epitope that determines G protein coupling specificity, suggesting that it is likely determined by a more complex three-dimensional network of interactions. Globally, the structure of the μOR-G_i complex is similar to the β_2AR-G_s, likely reflecting a similarity in the conformation of nucleotide-free states of Family A GPCR-G protein complexes. The primary interaction sites in both complexes occur between ICL2, ICL3 and TMs 3,5, and 6 on the receptor and the αN, αN-β1 loop, and α5 helix on the Gα subunit of the G protein (Fig. 4). The most striking difference between the β_2AR-G_s and μOR-G_i complex is in the relative position of the α5 helix of both G proteins, as well as the corresponding shift in the position of TM6 of the receptor. The α5 helix of $G\alpha_i$ is rotated ~21° relative to the α5 helix of $G\alpha_s$, leading to a 5 Å displacement of the extreme C-terminus of the $G\alpha_i$ helix α5 toward TM7 of the μOR (Fig. 4a). This difference in α5 positioning is associated with a smaller outward displacement of the μOR TM6. The C-terminal residues of α5 that interact with TMs 5 and 6 of the receptor are bulkier in G_s than in G_i, with Y and E compared to C and G at positions −4 and −3 from

the C-terminus, respectively. Accordingly, substitution of these two amino acids of G_s into G_i would lead to steric clashes with TM3 and the TM7-Helix 8 loop (Extended Data Fig. 7). In the G_s-coupled Family B calcitonin[11] and GLP-1[10] receptors, G protein coupling is associated with a large kink of TM6 at the conserved PxxG motif, which produces an even larger outward displacement of TM6 than what observed in the β_2AR-Gs complex.

Surprisingly, the structure of μOR-G_i shows substantial similarity to an active-state structure of the visual pigment rhodopsin (Meta II) in complex with a modified peptide derived from the 11 C-terminal residues of the α subunit of the visual G protein transducin ($G\alpha_t$CT2) (Extended Data Fig. 8)[28]. Despite the lack of the remainder of the heterotrimeric G protein in the MetaII- $G\alpha_t$CT2 structure, the conformation of TM6 of MetaII is highly similar to that of the μOR, while the location of the $G\alpha_t$CT2 peptide is almost identical to the C-terminus of G_i in complex with μOR. This finding is consistent with observations that substitution of the last five amino acids of the Gα α5 helix is sufficient to change G protein coupling specificity[29].

In Extended Data Table 2, we list amino acids in the μOR that interact with the cytoplasmic surface of G_i. The μOR ICL2 primarily forms interactions with the αN and α5 helices of $G\alpha_i$, including a key ionic interaction between the μOR D177$^{34.55}$ [G Protein Coupled Receptor Data Base (GPCRDB) numbering[30]] in ICL2 and R32 in the αN- β1 loop of $G\alpha_i$ (Fig. 4b). Although D$^{34.55}$ in ICL2 is conserved in all opioid receptors with available sequences (GPCRDB[31]), it is variable in most other G_i coupled receptors. Another notable interaction involves R179$^{34.57}$ in μOR ICL2, which simultaneously coordinates the highly conserved D164$^{3.49}$ in the DRY motif and potentially forms an additional interaction with D350 in the $G\alpha_i$ α5 helix (−5 position) (Fig. 4b). This arginine is essential for μOR induced G_i signaling, as the polymorphic variant R179C abolishes signaling *in vitro*[32] and leads to insensitivity to morphine in patients homozygous for the mutation[33]. The potential role of this interaction network in G protein coupling is supported by the preponderance of basic residues (arginine and lysine) at this position in most G_i coupled receptors, whereas G_s-coupled receptors employ alternative residues (Extended Data Table 2).

A further group of contacts occurs between P172$^{34.50}$ and V173$^{34.51}$ of μOR and a hydrophobic patch on $G\alpha_i$ comprised of residues F336, I343, I344, and T340 on the α5 helix and L194 on the β2- β3 loop (Fig. 4b, d). In the GDP bound state, these α5 helix residues are buried by the adjacent β2 and β3 loops. Coupling to a receptor involves an upward shift of the α5 helix and exposes these residues to form a shallow hydrophobic pocket that interacts with μOR V173$^{34.51}$ in ICL2 (Fig. 4b, d). In the case of G_s, a deeper hydrophobic pocket in this region engages the bulky aromatic F139$^{34.51}$ in ICL2 of the β_2AR (Fig. 4c, d).

In the μOR, ICL3 stabilizes the interface between receptor and G protein through two sets of interactions: one set involves multiple contacts with a hydrophobic patch on the α5 helix of $G\alpha_i$, while another engages the β6 strand of $G\alpha_i$ through a network of charged residues (Fig. 5a, b). The hydrophobic interface formed by ICL3 is similar in both the μOR and β_2AR; in the β_2AR, TM5 is helically extended to form a larger hydrophobic interaction around nonpolar residues in the α5 helix of $G\alpha_s$ (Fig. 5c, d). While the shorter ICL3 of the

μOR does not form a similar helical extension, it nevertheless fulfills the same role. Residues V262$^{5.68}$, M264 and L265 fold back to form a hydrophobic patch that interacts with hydrophobic residues on the α5 helix of $G\alpha_i$ (Figure 5a).

The second set of polar contacts involves μOR R263 and a backbone carbonyl to I319 on the β6 strand of $G\alpha_i$ (Fig. 5a). Mutations of R263 reduce, but do not abolish, G_i signaling[34], which is consistent with the potential importance of stabilizing the $G\alpha_i$ β6 strand in the observed conformation. A similar interaction is absent in the β_2AR-G_s complex (Fig. 5c). This additional recognition interface may be necessary for efficient μOR-G_i coupling due to the higher affinity for GDP to G_i relative to G_s. Compared to G_s-coupled receptors, additional interactions with the β6 strand in G_i-coupled receptors may be required to disrupt interactions between the Ras domain and GDP for efficient nucleotide exchange.

The cytosolic ends of μOR TMs 3,5 and 6 further stabilize the nucleotide-free conformation of the α5 helix by interacting with highly conserved residues in the distal C-terminus of $G\alpha_i$ (Figure 5b). In particular, C351 (−4 position) of $G\alpha_i$ is in close proximity to the cytosolic end of μOR TM3. This cysteine residue has previously been identified as the site of pertussis toxin-mediated inhibition of $G_{i/o}$ family proteins by enzymatic ADP-ribosylation[35]. The close apposition of C351 to the μOR cytoplasmic surface highlights how the addition of a bulky modification at this position can completely inhibit receptor coupling and nucleotide exchange[35]. In addition to this interaction, μOR residues M255$^{5.61}$, I278$^{6.33}$, M281$^{6.36}$, and V282$^{6.37}$ form a hydrophobic pocket that engages the absolutely conserved $G\alpha_i$ residue L353 (−2 position) in the α5 helix. Methionines M255$^{5.61}$ and M281$^{6.36}$ have previously been observed in NMR experiments to respond to activation by DAMGO[36], suggesting that this region undergoes conformational changes prior to G protein coupling. Further stabilization, however, is likely provided by a hydrogen bond between R277$^{6.32}$ and the backbone carbonyl of L353 (Fig. 5b). Notably, interactions between the C-terminus of the α5 helix and the receptor core are entirely different in the in the β_2AR-G_s complex (Fig. 5c).

Our findings provide structural insights into the inability of the μOR to couple to G_s, but do not explain the mechanism of G protein coupling specificity across all GPCRs. It is possible that coupling specificity is determined at an intermediate step in the formation of a GPCR-G protein complex, such as the initial interactions between the GDP-bound G protein and the agonist-bound receptor. Recent single molecule fluorescence studies provide evidence for a transient intermediate complex between GDP-bound G_s and the β_2AR that is associated with a smaller outward movement of TM6[37]. Previous studies suggest that amino acids C-terminal to helix 8 confer coupling specificity for G_q in the M_3 muscarinic receptor (M3R)[38]. Given that there are no interactions between the C-terminus of the β_2AR or μOR with their respective G proteins in the nucleotide-free complexes, we postulate that engagement of G_q and the M_3R C-terminus may occur at an earlier stage in complex formation. Thus, the nucleotide-free GPCR-G protein complex may be preceded by one or more GDP-bound intermediates characterized by dynamic low affinity interactions with the receptor. Such initial encounter complexes may have larger energetic differences for interactions with various G protein subtypes than the nucleotide-free state, and would thereby contribute more critically to coupling specificity. The transient nature of such

interactions, however, currently poses challenges for structure determination by both crystallography and cryo-EM.

METHODS

Online Methods

No statistical methods were used to predetermine sample size. The experiments were not randomized and the investigators were not blinded to allocation during experiments and outcome assessment.

Purification of μ-opioid receptor

These studies utilized a previously described mouse μOR construct with cleavable amino and carboxy terminal domains[12]. Briefly, the receptor was expressed in *Spodoptera frugiperda Sf9* insect cells using the baculovirus method (Expression Systems), extracted from insect cell membranes with n-dodecyl-β-D-maltoside (DDM, Anatrace), and purified by nickel-chelating sepharose chromatography. The Ni-NTA eluate was loaded onto M1 anti-FLAG immunoaffinity resin and washed with progressively lower concentrations of the antagonist naloxone. The μOR was then eluted in a buffer consisting of 20 mM Hepes pH 7.5, 100 mM NaCl, 0.1% DDM, 0.01% cholesterol hemisuccinate (CHS) supplemented with 50 nM naloxone, FLAG peptide and 5 mM EDTA. The monomeric fraction was purified by size exclusion chromatography on a Superdex 200 10/300 gel filtration column (GE) in 20 mM Hepes pH 7.5, 100 mM NaCl, 0.1% DDM, 0.01% CHS, and 1 μM DAMGO. A further 2-fold molar excess of DAMGO was added to the preparation and the resulting agonist-bound μOR preparation was concentrated to ~100 μM.

Expression and purification of heterotrimeric G_i

Heterotrimeric G_i was expressed and purified as previously described[24]. Briefly, *Trichuplusia ni Hi5* insect cells were coinfected with two viruses, one encoding the wild-type human $G\alpha_i$ subunit and another encoding the wild-type human $\beta_1\gamma_2$ subunits with an octahistidine tag inserted at the amino terminus of the β_1 subunit. Cultures were harvested 48 hours post infection. Cells were lysed in hypotonic buffer and lipid-modified heterotrimeric G_i was extracted in a buffer containing 1% sodium cholate. The soluble fraction was purified using Ni-NTA chromatography, and the detergent was exchanged from cholate to DDM on column. After elution, the protein was dialyzed against a buffer containing 20 mM Hepes pH 7.5, 100 mM NaCl, 0.015% DDM, 100 μM TCEP, 10 μM GDP, and concentrated to ~20 mg/mL for further complexing with the μOR.

Generation of scFv16

6–8 week old female Balb/c mice were immunized with a purified rhodopsin-G_i complex[39]. Hybridoma cells were prepared using splenocytes of immunized mice using standard methods in combination with PAI myeloma cells. Clones that showed a positive reaction to purified rhodopsin(N2C/D282C/M257Y)/G_{i1} complex in an ELISA assay and by immunoprecipitation were further characterized as monoclonal antibodies or Fab fragments. Fab-16 was selected from the initial pool of clones because it prevented dissociation of the rhodopsin (N2C/D282C/M257Y)/Gi1 complex by GTPγS, and therefore acted as a

stabilizing chaperone in the same manner as Nb35 for Gs. The full sequence of constructs used is listed in Supplemental Figure 1. All animal studies were performed at Roche Innovation Center Basel according to ethical guidelines. All cell lines were obtained from manufacturer and tested for contamination.

A carboxy-terminal hexahistidine-tagged single chain construct of Fab16 (scFv16) was cloned into a modified pVL1392 vector containing a GP67 secretion signal immediately prior to the amino terminus of the scFv, expressed in secreted form from *Trichuplusia ni Hi5* insect cells using the baculoviral method, and purified by Ni-NTA chromatography. Supernatant from baculoviral infected cells was pH balanced by addition of Tris pH 8.0. Chelating agents were quenched by addition of 1 mM nickel chloride and 5 mM calcium chloride and incubation with stirring for 1 hr at 25 °C. Resulting precipitates were removed by centrifugation and the supernatant was loaded onto Ni-NTA resin. The column was washed with 20 mM Hepes pH 7.5, 500 mM NaCl, and 10 mM imidazole followed by a low salt wash comprised of the same buffer substituted with 100 mM NaCl. Following elution with the same buffer supplemented with 250 mM imidazole, the carboxy-terminal hexahistidine tag was cleaved by incubation with human rhinovirus 3C protease, and the protein was dialyzed into a buffer consisting of 20mM Hepes pH 7.5 and 100 mM NaCl. Cleaved scFv16 was further purified by reloading over Ni-NTA resin. The flow-through was collected and purified over gel filtration chromatography using a Superdex 200 16/60 column. Monomeric fractions were pooled, concentrated, and flash frozen in liquid nitrogen until further use.

Formation and purification of the μOR-G_i-scFv16 complex

Purified DAMGO-bound μOR was mixed with a 1.2 molar excess of G_i heterotrimer. The coupling reaction was allowed to proceed at 24 °C for 1 hour and was followed by addition of apyrase to catalyze hydrolysis of unbound GDP, which destabilizes the nucleotide-free complex[40]. After one more hour at 25 °C, a 4-fold volume of 20 mM Hepes pH 7.5, 100 mM NaCl, 1% lauryl maltose neopentyl glycol (L-MNG), 0.1% CHS was added to the complexing reaction to initiate detergent exchange. After one hour incubation at 25 °C to allow micelle exchange, 1 mM $MnCl_2$ and lambda phosphatase (New England Biolabs) were added to dephosphorylate the preparation. This reaction was further incubated at 4 °C for 2 hours. To remove excess G protein and residual DDM, the complexing mixture was purified by M1 anti-FLAG affinity chromatography. Bound complex was first washed in a buffer containing 1% L-MNG, followed by washes in gradually decreasing L-MNG concentrations. The complex was then eluted in 20mM Hepes pH 7.5, 100mM NaCl, 0.01% MNG/0.001% CHS, 300 nM DAMGO, 5 mM EDTA, and FLAG peptide. The eluted complex was supplemented with 100 μM TCEP to provide a reducing environment. The tobacco etch virus (TEV) protease and human rhinovirus 3C protease were added to cleave the flexible μOR amino- and carboxy- termini. Finally, a 1.2 molar excess of scFv16 was added to the preparation. Once cleavage of the termini was confirmed by SDS-PAGE, the μOR-G_i-scFv16 complex was purified by size exclusion chromatography on a Superdex 200 10/300 column in 20mM Hepes pH 7.5, 100mM NaCl, 300 nM DAMGO, 0.00075% MNG and 000025% GDN. Peak fractions were concentrated to ~7 mg/mL for electron microscopy studies.

Cryo-electron microscopy of μOR-G_i-scFv16 complex

3.0 μL of purified μOR-G_i-scFv16 complex was applied to glow-discharged 200 mesh grids (Quantifoil R1.2/1.3) and subsequently vitrified using a Vitrobot Mark IV (Thermo Fischer Scientific). Cryo-EM imaging was performed on a Titan Krios operated at 300 kV at a nominal magnification of 130,000x using a Gatan K2 Summit direct electron camera in counted mode, corresponding to a pixel size of 1.04 Å. A total of 2642 image stacks were obtained with a defocus range of −0.8 to −2.6 μm. Each stack movie was recorded for a total of 8 seconds with 0.1s per frame. The dose rate was 5 e/Å^2/s, resulting in an accumulated dose of 40 electrons per Å^2.

Dose fractionated image stacks were subjected to beam-induced motion correction using MotionCor2[41]. A sum of all frames, filtered according to exposure dose, in each image stack was used for further processing. CTF parameters for each micrograph were determined by Gctf v1.06[42]. Particle selection, two-dimensional and three-dimensional classification, and 3D reconstruction were performed using RELION2.1[43], apart from the last round of local refinement and reconstruction that was performed with Frealign[44]. Semi-automated selected 893,426 particle projections were subjected to reference-free two-dimensional classification and averaging using a binned data set with a pixel size of 2.08 Å. 379,373 particles belonging to well-defined averages were subjected to further processing. An *ab initio* map generated by VIPER[45] was used as initial reference model for maximum-likelihood-based three-dimensional classification, which, however did not produce classes with notable differences. Thus, all 379,373 particle projections were subjected to 3D refinement, producing a map at 4.3 Å resolution. The dataset was further reduced by removing particle projections from micrographs with resolution lower than 4.5 Å, resulting in a data set of 359,406 particles that were subjected to refinement and reconstruction after subtracting densities for the mobile Gα α-helical domain and the detergent micelle[11]. Particle projection assignments from RELION were imported into Frealign[46] for a final round of local refinement and reconstruction. To prevent overfitting, the resolution limit for every alignment iteration never exceeded the 0.9 value of the Frealign calculated FSC. The map was further improved map after additionally subtracting densities corresponding to the ScFv from the raw particle projections[11]. The indicated resolution, using Phenix “gold standard” FSC[47], of the final reconstruction is 3.5 Å and 3.6 Å at FSC 0.143 for the ScFv subtracted map and the ScFv including map, respectively. Local resolution was determined using the Bsoft package[48] with unfiltered half-maps as input.

Model Building and Refinement

The building of a full atomic model for the μOR-G_i complex was aided by the quality and resolution of our map, as well as the existence of high-resolution crystal structures of each of the components that make up the complex. A composite model was formed by rigid body fitting of the active-state μOR (PDB ID: 5C1M)[12] with nanobody removed, as well as the Ras domain and βγ subunits of GDP-bound G_i (PDB ID: 1GP2)[23]. The α5 helix of $G\alpha_i$ was removed and manually fit to the density, and the final 8 residues missing from the extreme C-terminus of the 1GP2 structure were manually built in coot[49]. This starting model was then subjected to iterative rounds of automated refinement in Rosetta[50] and Phenix real space refine[47], and manual building in Coot[49]. In the regions of the model for which side

chain density was too weak to unambiguously assign a conformation, we stubbed residues to their C βposition, while preserving sequence information (Supplemental Figure 2,3). The final model was visually inspected for general fit to the map, and geometry was further evaluated using Molprobity[51] as part of the Phenix suite of software. Initial restraints for DAMGO were generated using the PRODRG server[52]. To further refine the pose of DAMGO, we chose a pose from molecular dynamics simulation consistent with our map and then performed a refinement using Phenix. This involved manually editing the residue and atom names from a CHARMM parameter file to match the 3-letter codes and atom names from the rcsb. In particular, DAL for D-alanine, MEA for N-methyl phenylalanine, and ETA for Gly-ol C terminus. Additional, custom, restraints were generated to keep planarity of the final peptide bond between MEA and ETA as a supplement to the natural library of phenix amino acid restraints. Model overfitting was evaluated through its refinement against one cryo-EM half map after randomly displacing all atoms by 0.2 Å. FSC curves were calculated between the resulting model and the half map used for refinement (green curve, Extended Data Fig. 2b, c), as well as between the resulting model and the other half map for cross- validation (blue curve, Extended Data Fig. 2b, c), and also against the full map (red curve, Extended Data Fig. 2b, c). The final refinement statistics for both models are provided in Extended Data Table 1.

System setup for molecular dynamics simulations

Molecular dynamics simulations were initiated from an earlier refinement of the structure reported in this study after removing the G protein and ScFv fragment. Prior to beginning simulations, Schrödinger Glide[53] was used to relax DAMGO to an energetically favorable conformation. The initial DAMGO pose is depicted in Extended Data Figure 3. We performed five independent simulations, for each of which initial atom velocities were assigned randomly and independently. Prime (Schrödinger, Inc.) was used to model missing side chains, and neutral acetyl and methylamide groups were added to cap protein termini. Titratable residues remained in their dominant protonation state at pH 7, as determined using PropKa, except for $D^{2.50}$ and $D^{3.49}$ which were protonated. Our simulations incorporated the waters from the 5C1M crystal structure.

The prepared protein structures were aligned to the Orientation of Proteins in Membranes (OPM) structure for PDB entry 5C1M[54]. The aligned structures were then inserted into a pre-equilibrated palmitoyl-oleoyl-phosphatidylcholine (POPC) bilayer using Dabble, a simulation preparation software[55]. Sodium and chloride ions were added to neutralize each system at a concentration of approximately 150 mM. Bilayer dimensions were chosen to maintain at least a 30 Å buffer between protein images in the x-y plane and a 20 Å buffer between protein images in the z direction. Final system dimensions were approximately 80 × 75 × 90 $Å^3$. Simulation times for each replicate were approximately 1 μs.

Molecular dynamics simulation protocols

We used the CHARMM36m force field for proteins, lipids, and ions and the TIP3P model for waters[56–60]. Parameters for the non-canonical residues in DAMGO were determined by analogy to N-methyl glycine for assigning N-methyl parameters to N-methyl phenylalanine (residue 4) and by analogy to serine to assign parameters to the Gly-ol capping group

(residue 5). CMAP terms for D-alanine were inverted from those for L-Alanine to account for the inverted chirality of the residue.

We performed the simulations using the Compute Unified Device Architecture (CUDA) version of Particle-Mesh Ewald Molecular Dynamics (PMEMD) in AMBER on one or two graphical processing units (GPUs)[61]. Simulations were performed using the AMBER16[62] software. Three rounds of minimization were performed, each consisting of 500 iterations of steepest descent minimization, followed by 500 iterations of conjugate gradient descent minimization, with harmonic restraints of 10.0, 5.0, and 1.0·kcal·mol^{-1}·Å^{-2} placed on the protein and lipids. Systems were heated from 0K to 100K in the NVT ensemble over 12.5 ps and then from 100K to 310K in the NPT ensemble over 125 ps, using 10.0·kcal·mol^{-1}·Å^{-2} harmonic restraints applied to lipid and protein heavy atoms. Systems were then equilibrated at 310 K in the NPT ensemble at 1 bar, with harmonic restraints on all protein heavy atoms tapered off by 1.0 kcal·mol^{-1}·Å^{-2} starting at 5.0·kcal·mol^{-1}·Å^{-2} in a stepwise fashion every 2 ns for 10 ns and then by 0.1 kcal·mol^{-1}·Å^{-2} in a stepwise fashion every 2 ns for 20 ns. Production simulations were performed in the NPT ensemble at 310K and 1 bar, using a Langevin thermostat for temperature coupling and a Monte Carlo barostat for pressure coupling. These simulations used a 4 fs time step with hydrogen mass repartitioning[63]. Bond lengths to hydrogen atoms were constrained using SHAKE. Simulations used periodic boundary conditions. Non-bonded interactions were cut off at 9.0 Å, and long-range electrostatic interactions were computed using Particle Mesh Ewald (PME) with an Ewald coefficient of approximately 0.31 Å and an interpolation order of 4. The FFT grid size was chosen such that the width of a grid cell was approximately 1 Å.

During production simulations, all residues within 5 Å of the G protein interface were restrained to the initial structure using 5.0 kcal·mol^{-1}·Å^{-2} harmonic restraints applied to non-hydrogen atoms. Using such restraints reduces the overall system size, enabling more simulation, while ensuring that the receptor maintains an active conformation throughout the simulation.

Analysis protocols for MD simulation

Trajectory snapshots were saved every 200 ps during production simulations. The AmberTools17 CPPTRAJ package was used to reimage and center trajectories[64]. Simulations were visualized and analyzed using Visual Molecular Dynamics (VMD)[65]. In two simulations, DAMGO was trapped in an unstable binding pose, wherein the water-mediated interaction between the DAMGO Tyr residue and His297 failed to form during equilibration, and instead a direct hydrogen bond between these residues was formed. Our analysis is based on the other three simulations, in which DAMGO's pose was consistent with the EM density. Water occupancy maps were generated using AmberTools17 GIST[66,67]. Frames from every 1 ns of simulation, excluding the first 400 ns, aligned to the initial structure, were used as input. The grid size was set to 0.25 Å. The resulting map was smoothed using a Gaussian filter with a standard deviation of 2 grid cells.

Extended Data

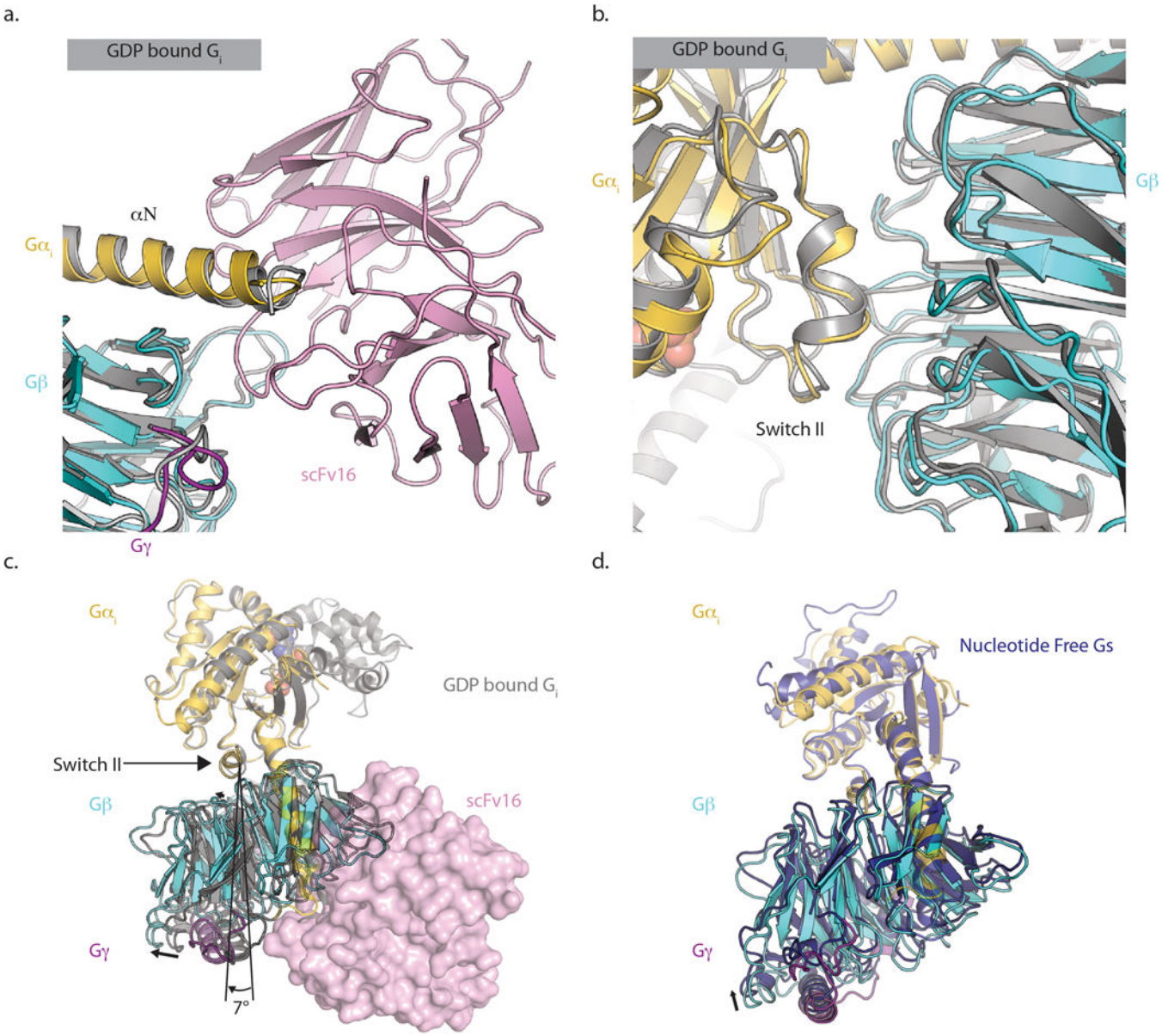

Extended Data Figure 1. scFv binding characteristics

scFv 16 does not perturb the interfaces between Gα and Gβ at **a)** its binding epitope or **b)** the Switch II region located ~40A away. Our structure is colored by chain, while the structure of GDP-bound G_{i1} heterotrimer (PDB 1GP2) is colored grey. c) In the nucleotide-free state, there is a ~7˚ rotation of G βγ relative to the $G\alpha_s$ Switch II domain when compared to the GDP-bound form. This rotated conformation is similar to that observed in nucleotide-free G_s coupled to the β_2AR (PDB ID 3SN6) as shown in panel **d)**.

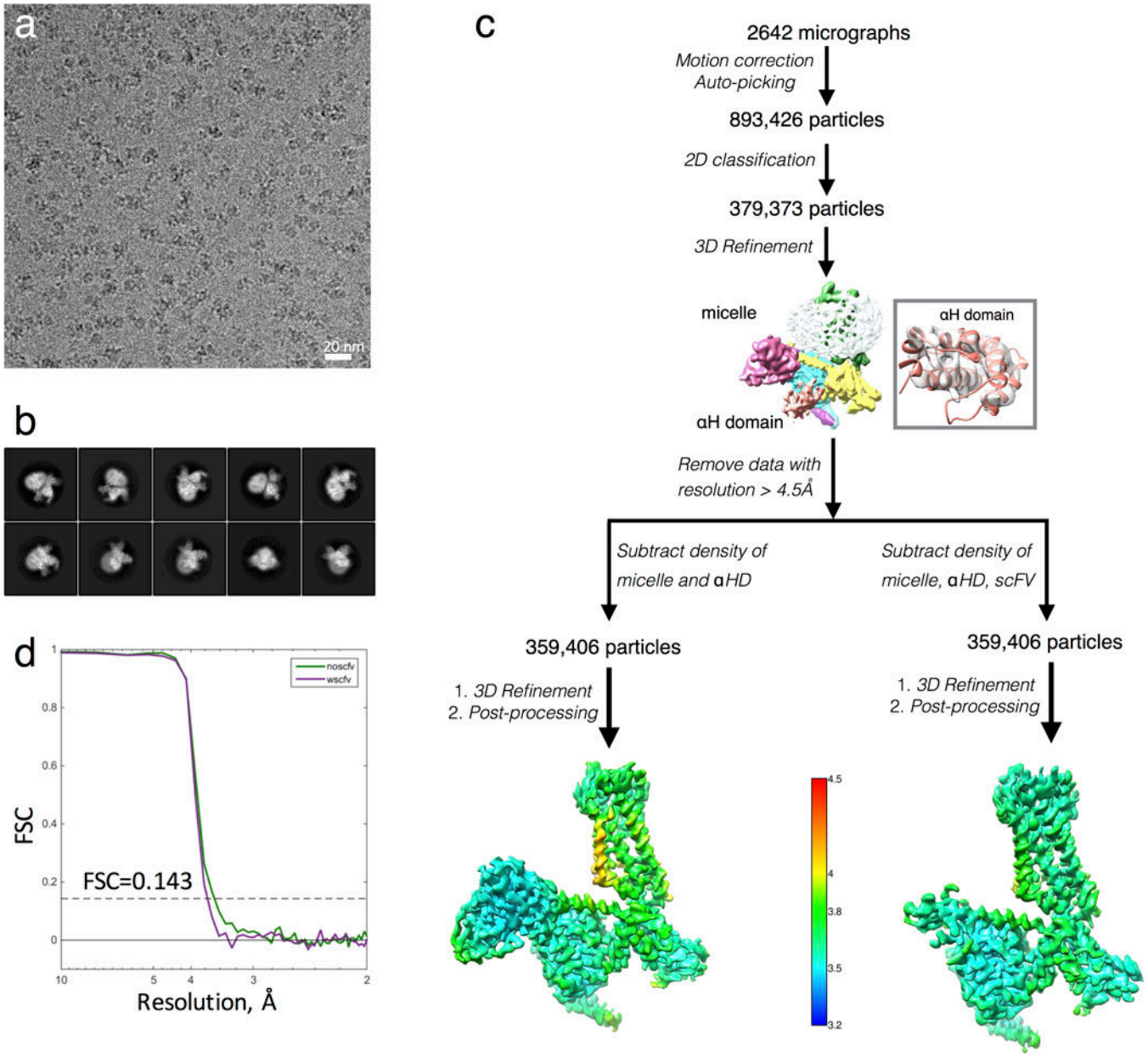

Extended Data Figure 2. Cryo-EM data processing

a, Representative cryo-EM micrograph of the μOR-G_i complex. Scale bar, 20nm.

b, Representative two-dimensional averages showing distinct secondary structure features from different views of the complex.

c, Flow chart of cryo-EM data processing. The unmasked map in the middle of the chart has been colored by subunit. The inset shows the fit of the crystal structure of the α-helical domain in the corresponding density of the unmasked reconstruction. Three-dimensional density maps colored according to local resolution.

d, "Gold standard" Fourier shell correlation (FSC) curves from Phenix indicates overall nominal resolutions of 3.5 Å and 3.6 Å using the FSC=0.143 criterion for the scFv-subtracted map (green curve) and scFv-retained maps (purple curve), respectively.

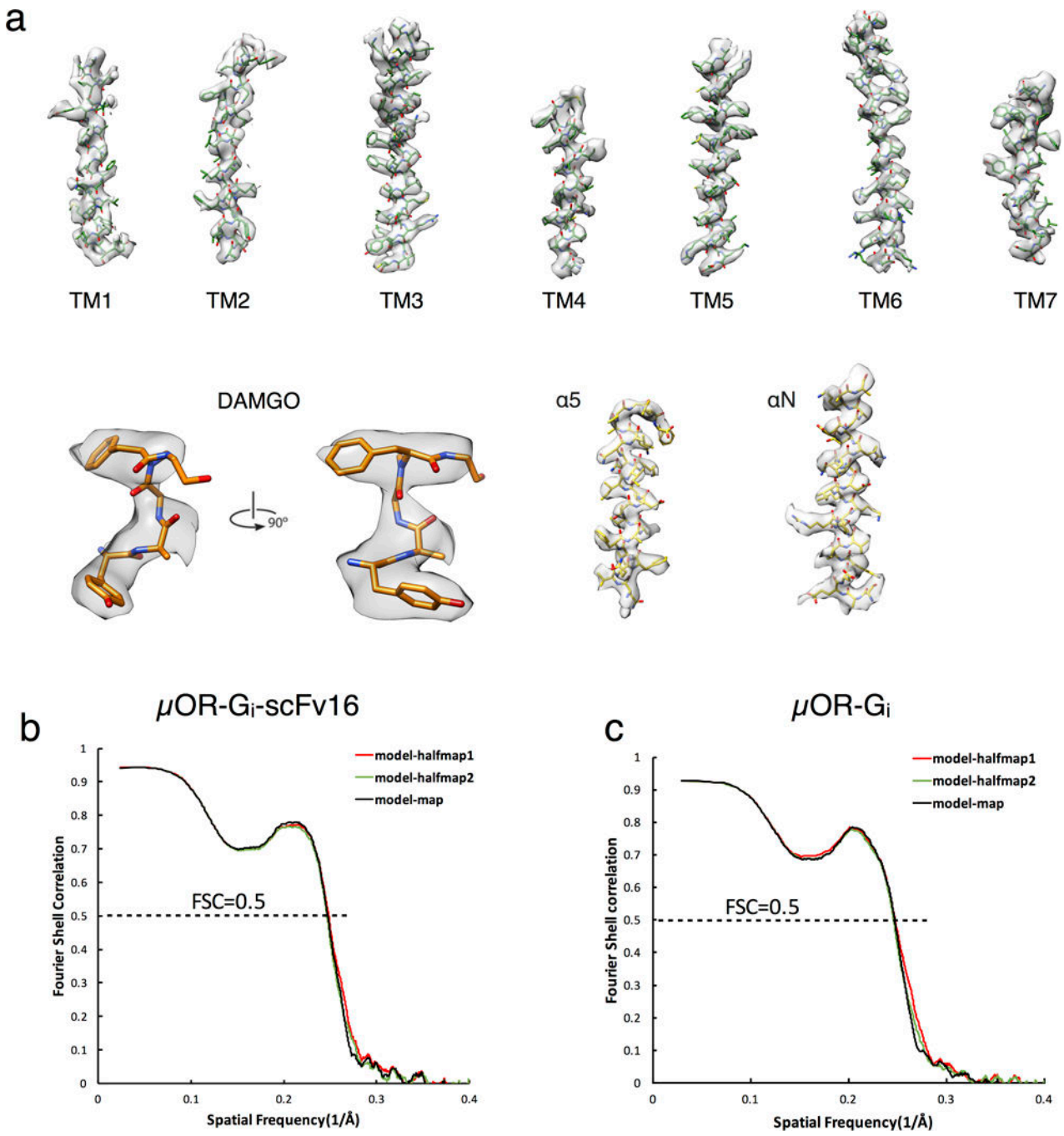

Extended Data Figure 3. Cryo-EM map vs. refined structure

a) EM density map (scFv subtracted) and model are shown for all seven transmembrane α-helices of the μOR, DAMGO, and Gα helices α5 and αN.

b,c) Cross-validation of model to EM density map. The model was refined against one half map after displacement of atoms by 0.2A, and FSC curves were calculated between this model and the final cryo-EM map (full dataset, black), of the outcome of model refinement with a half map versus the same map (red), and of the outcome of model refinement with a

half map versus the other half map (green). The results of the scFv-retained model vs. map and of scFv subtracted model vs. map are shown in **b)** and **c)**, respectively.

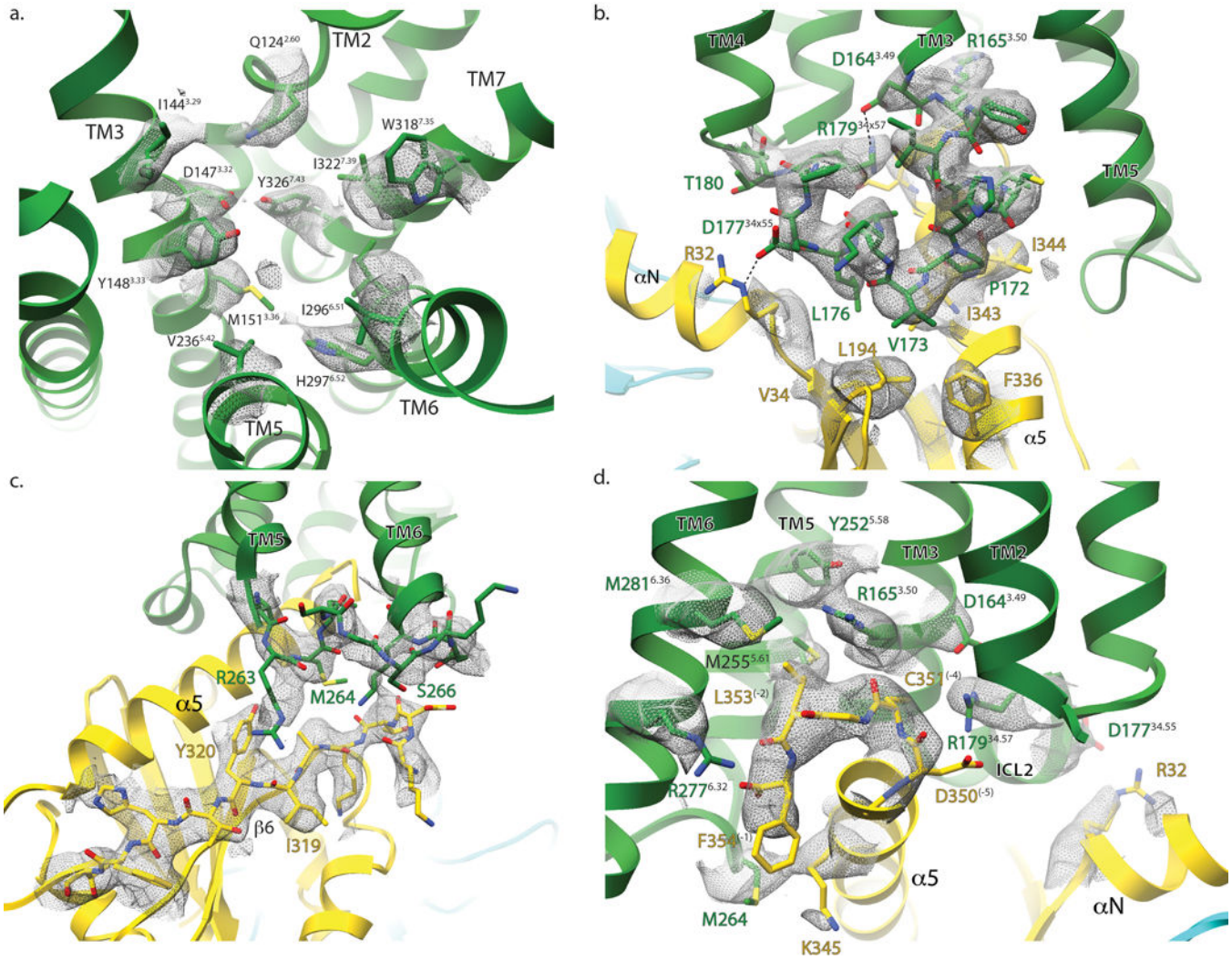

Extended Data Figure 4. Selected cryo-EM densities of μOR-G_i Complex

Cryo-EM density (displayed as mesh) surrounding residues involved in **a**) DAMGO binding, **b**) μOR-$Gα_i$ interaction around ICL2, **c**) ICL3, and **d**) cytoplasmic ends of the μOR transmembrane helices. These figures accompany the models shown in figures 1e, 4b, 5a, and 5b respectively.

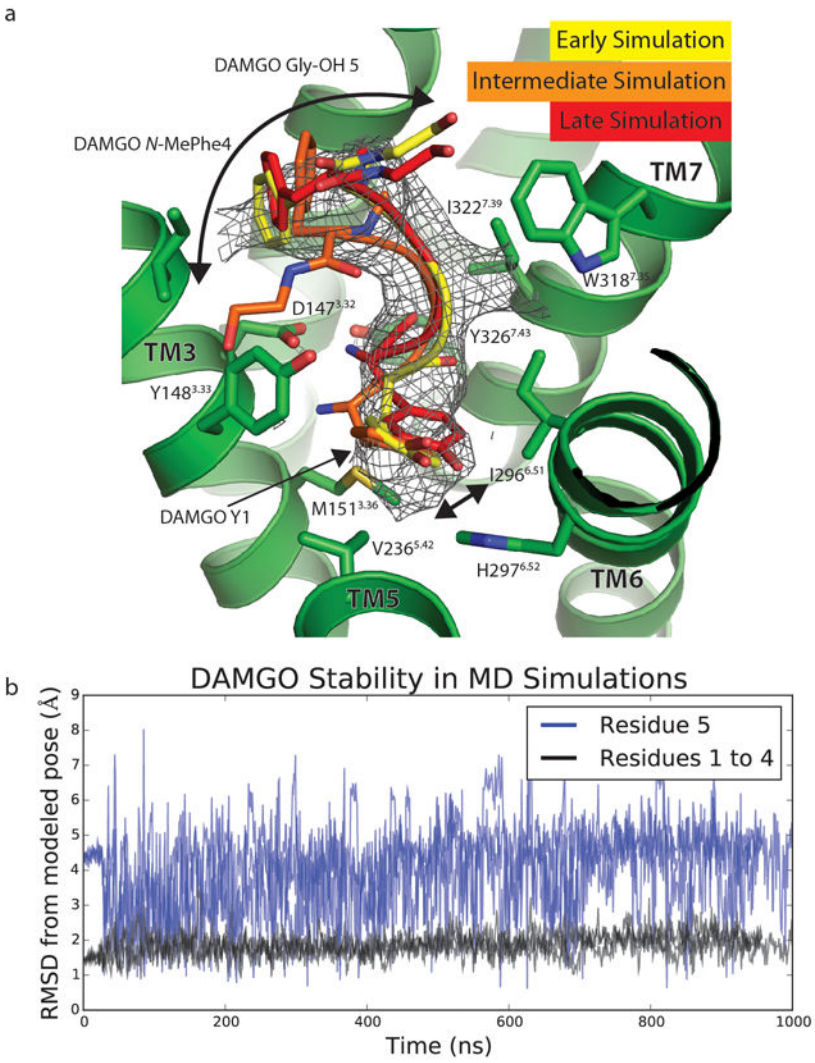

Extended Data Figure 5. Stability of DAMGO in MD Simulations

a. Over the course of MD simulations, the positions of the first 4 residues of DAMGO do not significantly change, while the 5th residue (Gly-ol) shows significant variability in position. Frames from the first and last 100 ns are shown with an intermediate to highlight both the relative stability of the first 4 amino acids, as well as the flexibility of the fifth. Arrows show the extent of motion in the N- and C-terminal residues over the course of simulation. Cryo-EM density for DAMGO is shown as mesh.

b. Root mean standard deviations (RMSDs) from the modeled pose of DAMGO to the pose during MD simulations. The RMSD calculations include heavy atoms on the peptide backbone. Data from three independent simulations are plotted. The RMSDs for residues 1 to 4 (black) and the C-terminal Gly-ol (blue) are plotted separately to highlight their stability and mobility, respectfully.

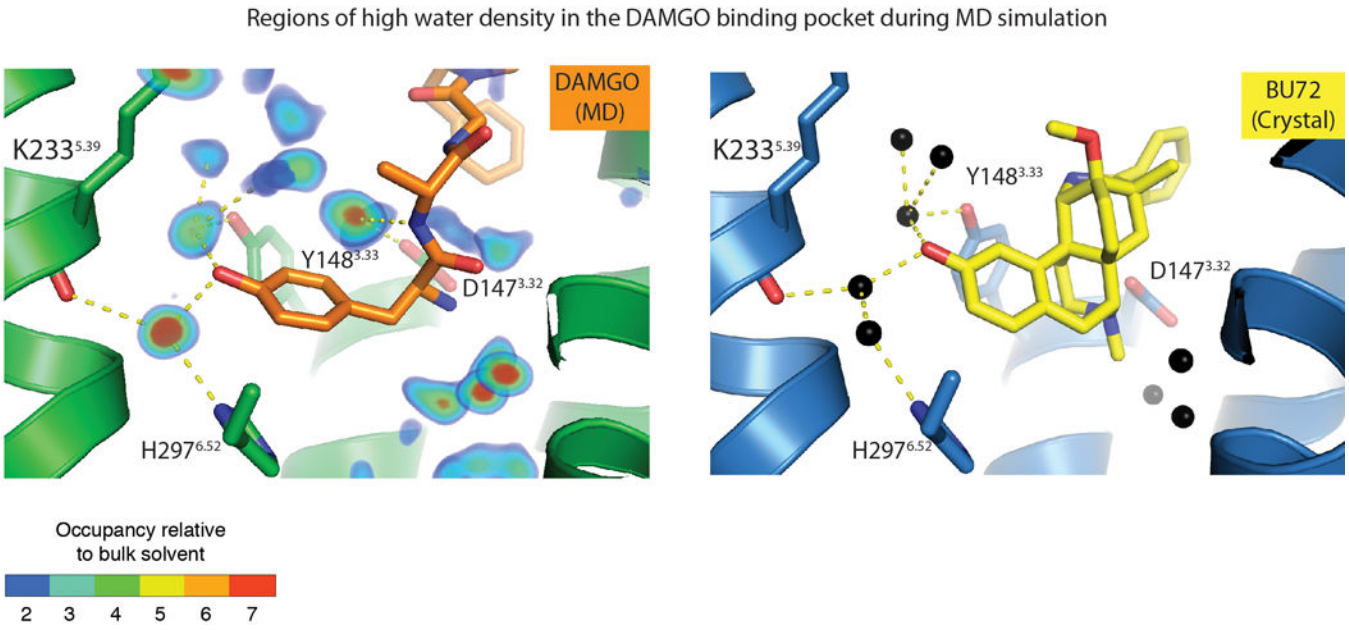

Extended Data Figure 6. Water occupancy in orthosteric binding site

Left panel, water occupancy in MD simulations of DAMGO-bound μOR overlaid with a representative conformation from MD simulations. 'Occupancy relative to bulk solvent' is the ratio of the rate at which water is observed in a given volume to the rate at which water is expected to be observed in an equivalent volume in the bulk solvent. For example, blue regions (occupancy ratio = 2) are occupied by water twice as often as an equivalent region in the bulk solvent. **Right panel**, crystallographic waters in the BU72-bound μOR binding pocket (PDB ID: 5C1M). Waters are shown as black spheres, BU72 is shown as yellow sticks, and hydrogen bonds are shown as dashed lines.

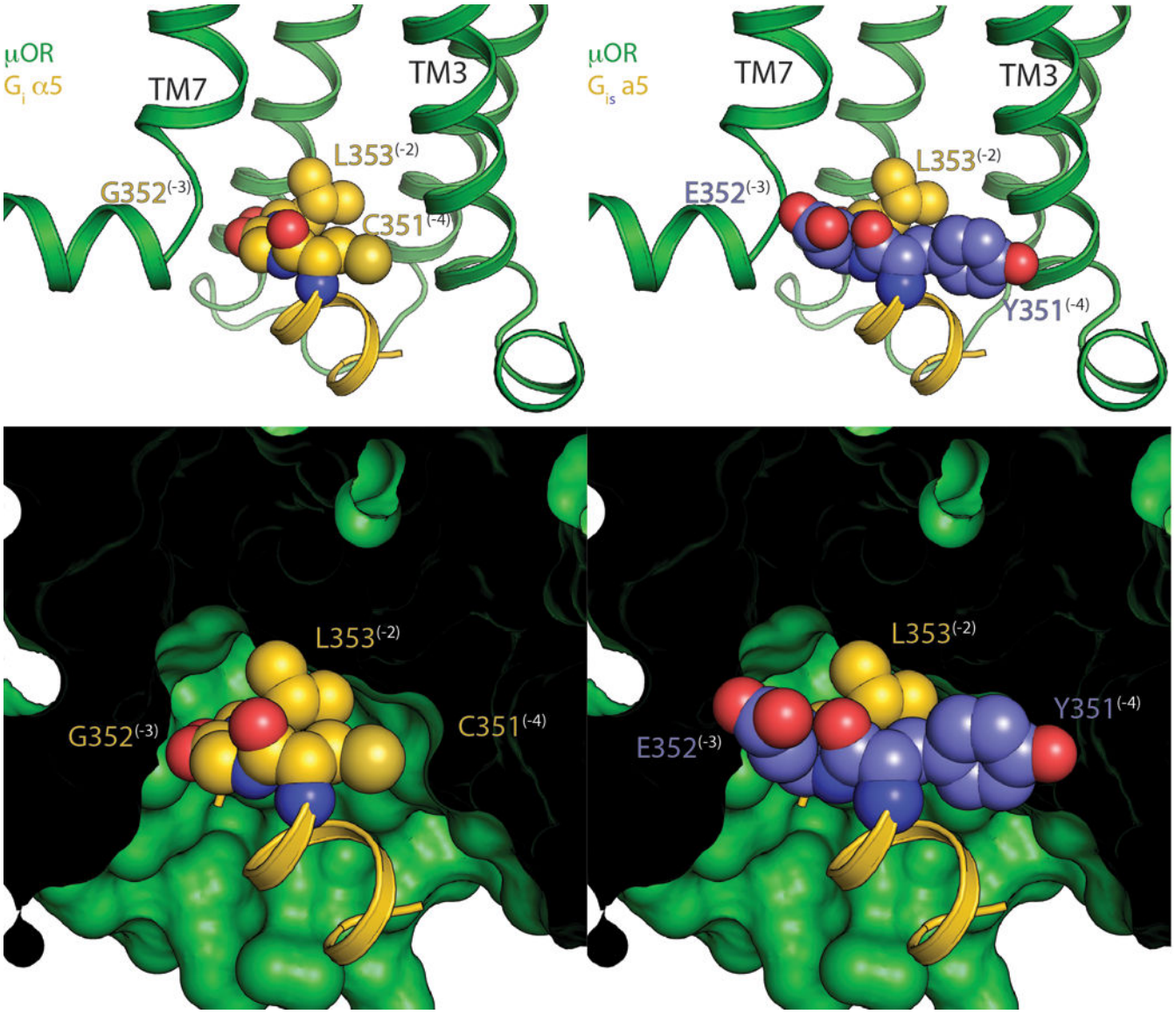

Extended Data Figure 7. Comparison of the C-termini of $G\alpha_s$ and $G\alpha_i$

The C-terminus of $G\alpha_s$ is bulkier than that of $G\alpha_i$ due to substitution of small amino acids C (−4 position) and G (−3 position) in $G\alpha_i$ to Y and E respectively in $G\alpha_s$. This leads to steric clashes with TMs 3 and 7 of the μOR.

Top - ribbon view of μOR (green) with WT $G\alpha_i$ (gold, left) and a $G\alpha_{is}$ model (right) created by substituting C and G for Y and E based on the β_2AR-G_s crystal structure. Substituted positions are colored in light purple. The −4 to −2 positions have their side chains shown as spheres, and the rest as a ribbon.

Bottom - space filling view of the μOR showing the steric clashes that result from these substitutions.

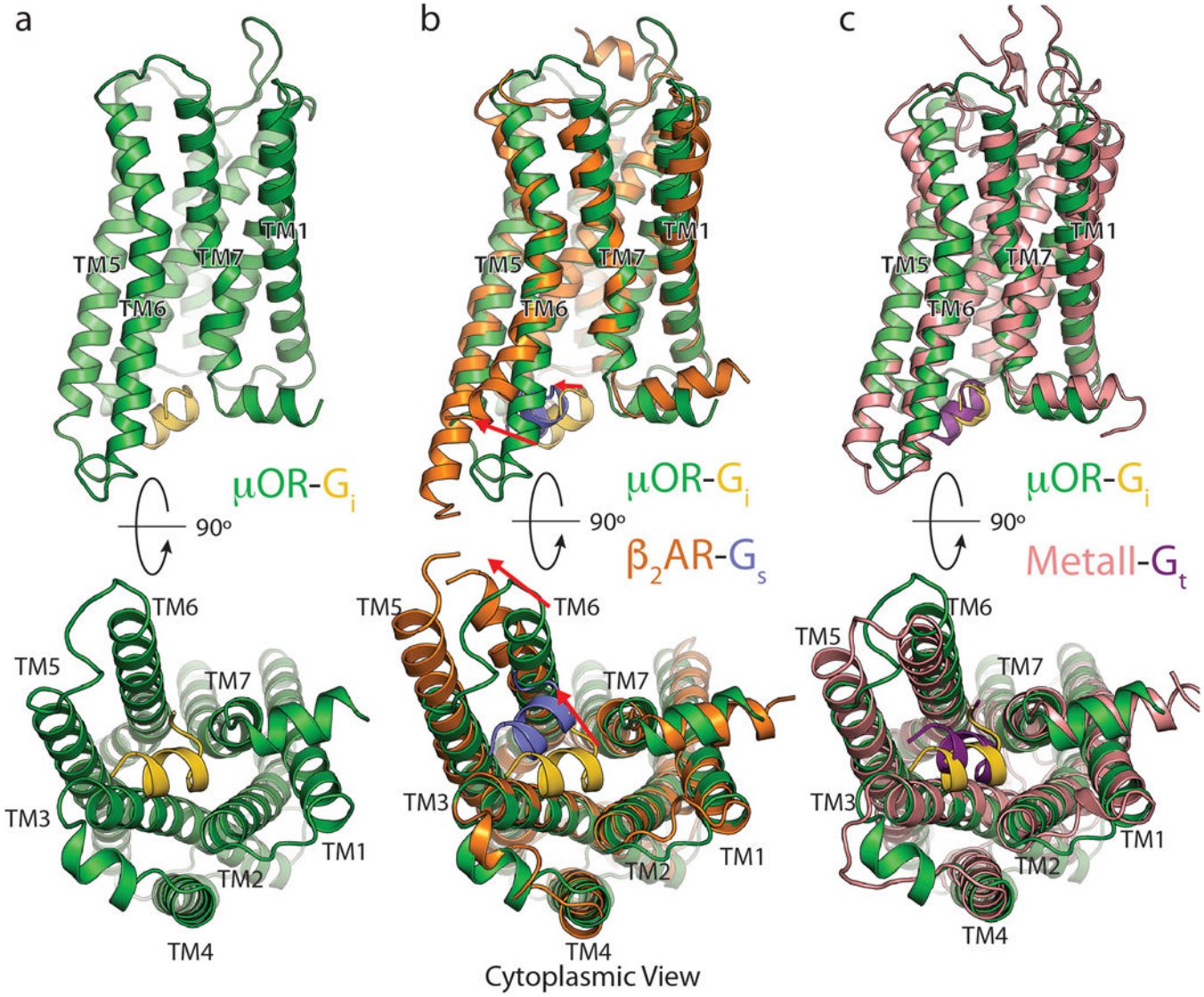

Extended Data Figure 8. Comparison of Gai C terminal peptide binding modes

Side (top half), and cytoplasmic (bottom half) views of **a**) the μOR (green) with the last 11 residues of $G\alpha_i$ (gold) alone, **b**) compared to the β_2AR(orange) with the last 11 residues of $G\alpha_s$ (light purple) (PDB ID 3SN6), or **c**) compared to MetaII Rhodopsin (pink) in complex with an 11 residue $G_{transducin}$ (G_t) C-terminal peptide (dark purple) (PDB ID 3PQR). The mOR-Gi complex aligns best with the MetaII-G_t complex both in terms of TM6 displacement as well as position of the α5 peptide.

Extended Data Table 1

Cryo-EM data collection, refinement and validation statistics

	μOR-G_i Complex (EMDB-xxxx) (PDB xxxx)	μOR-G_i-scFvl6 Complex (EMDB-yyyy) (PDB yyyy)
Data collection and processing		

	μOR-G_i Complex (EMDB-xxxx) (PDB xxxx)	**μOR-G_i-scFvl6 Complex (EMDB-yyyy) (PDB yyyy)**
Magnification	48,076	48,076
Voltage (kV)	300	300
Electron exposure (e–/Å^2)	40	40
Defocus range (μm)	−0.8 ~ −2.6	−0.8 ~ −2.6
Pixel size (Å)	1.04	1.04
Symmetry imposed	C1	C1
Initial particle images (no.)	893,426	893,426
Final particle images (no.)	359,406	359,406
Map resolution (Å)	3.5 Å	3.6 Å
FSC threshold	(0.143)	(0.143)
Map resolution range (Å)	3.3-4.5	3.3-4.5
Refinement		
Initial model used (PDB code)	5C1M 1GP2	5C1M 1GP2
Model resolution (Å)	3.5	3.6
Model resolution range (Å)	3.3-4.5	3.3-4.5
Map sharpening *B* factor (Å^2)	Pre −90, post −60	Pre −90, post −60
Model composition		
Non-hydrogen atoms	6986	8731
Protein residues	886 residues (6949 atoms)	1119 residues (8694 atoms)
Ligands	1 (37 atoms)	1 (37 atoms)
B factors (Å^2)		
Protein	33.23	60.55
Ligand	31.27	79.99
R.m.s. deviations		
Bond lengths (Å)	0.007	0.007
Bond angles (°)	1.311	1.015
Validation		
MolProbity score	1.89	1.89
Clashscore	7.02	8.16
Poor rotamers (%)	0.72	0.92
Ramachandran plot		
Favored (%)	91.54	92.93
Allowed (%)	8.35	6.98
Disallowed (%)	0.11%	0.09%

Extended Data Table 2

Sequence alignment of residues that form the interaction interface between μOR and G_i. Receptors from different branches of the GPCR family with different coupling specificity were selected for analysis. Sequences and alignment were performed using GPCRDB (gpcrdb.org)

	Coupling	Branch											
mOR Residue			T103	V169	P172	V173	D177	R179	T180	M255	K271	R277	I278
			2.39	3.54	34.50	34.51	34.55	34.57	4.38	5.61	6.26	6.32	6.33
[Human] 5-HT1A receptor	Gi	α	A	I	P	I	N	R	T	I	A	K	T
[Human] 5-HT1B receptor	Gi	α	A	I	A	V	A	R	T	I	M	K	A
[Human] M2 receptor	Gi	α	N	V	P	L	V	R	T	I	P	K	V
[Human] M4 receptor	Gi	α	N	V	P	L	A	R	T	I	M	K	V
[Human] alpha2A-adrenoceptor	Gi	α	Q	I	A	I	L	R	T	I	R	R	F
[Human] FPR1	Gi	γ	T	V	P	V	N	R	T	I	–	R	P
[Human] FPR2/ALX	Gi	γ	T	V	P	V	N	R	T	I	–	R	P
[Human] GAL1 receptor	Gi	γ	T	I	S	R	S	R	V	V	–	K	T
[Human] GAL3 receptor	Gi	γ	T	V	P	L	A	R	T	T	R	R	A
[Human] δ receptor	Gi	γ	T	V	P	V	D	R	T	M	K	R	I
[Human] κ receptor	Gi	γ	T	V	P	V	D	R	T	M	K	R	I
[Human] μ receptor	Gi	γ	T	V	P	V	D	R	T	M	K	R	I
[Human] NOP receptor	Gi	γ	T	I	P	I	D	R	T	M	K	R	I
[Human] SST1 receptor	Gi	γ	T	V	P	I	R	R	R	I	R	K	I
[Human] SST2 receptor	Gi	γ	T	V	P	I	K	R	R	I	R	K	V
[Human] SST3 receptor	Gi	γ	T	V	P	T	R	R	T	I	R	R	V
[Human] SST4 receptor	Gi	γ	T	V	P	L	T	R	R	I	R	K	I
[Human] SST5 receptor	Gi	γ	T	V	P	L	R	R	R	I	–	K	V
[Human] CCR1	Gi	γ	T	I	A	V	R	R	T	I	–	K	A
[Human] CCR4	Gi	γ	T	I	A	V	R	R	T	I	–	K	A
[Human] CXCR4	Gi	γ	T	I	A	T	R	R	K	I	–	K	A
[Human] A1 receptor	Gi	α	T	V	P	L	M	V	T	V	Y	K	I
[Human] beta1-adrenoceptor	Gs	α	T	I	P	F	S	L	T	V	V	K	A
[Human] beta2-adrenoceptor	Gs	α	T	I	P	F	S	L	T	V	F	K	A
[Human] MC1 receptor	Gs	α	M	I	A	L	S	V	T	G	–	K	G
[Human] MC2 receptor	Gs	α	M	I	A	L	S	V	T	K	–	K	G
[Human] MC4 receptor	Gs	α	M	I	A	L	N	M	T	R	–	K	G
[Human] A2A receptor	Gs	α	T	I	P	L	G	V	T	I	T	H	A
[Human] H2 receptor	Gs	α	T	V	P	L	V	V	T	I	A	K	A
[Human] TA1 receptor	Gs	α	T	V	P	L	A	M	N	I	S	K	A
[Human] RXFP1	Gs	δ	Y	I	P	F	R	–	G	M	Q	I	L
[Human] RXFP2	Gs	δ	H	I	P	F	R	–	G	M	C	A	V
[Human] V2 receptor	Gs	β	I	I	P	M	R	G	S	I	V	K	T
[Human] 5-HT2A receptor	Gq	α	T	I	P	I	R	N	S	T	S	K	A
[Human] 5-HT2B receptor	Gq	α	T	I	P	I	Q	N	S	T	T	R	A
[Human] M1 receptor	Gq	α	N	V	P	L	A	R	T	I	S	K	A

	Coupling	Branch											
[Human] M3 receptor	Gq	α	N	I	P	L	A	R	T	I	S	K	A
[Human] M5 receptor	Gq	α	N	I	P	L	A	R	T	I	V	K	A
[Human] alpha1A-adrenoceptor	Gq	α	T	V	P	L	T	V	T	V	K	K	A
[Human] GAL2 receptor	Gq	γ	T	I	P	L	E	R	T	T	A	K	V
[Human] OX1 receptor	Gq	β	T	I	P	L	–	–	T	I	Q	K	T
[Human] OX2 receptor	Gq	β	T	I	P	L	–	–	T	I	Q	K	T
[Human] NK1 receptor	Gq	β	T	I	–	–	–	–	S	V	Q	K	V

Supplementary Material

Refer to Web version on PubMed Central for supplementary material.

Acknowledgments

We thank Jean-Philippe Carralot (F. Hoffmann-La Roche Ltd) for help in antibody generation, Craig Yoshioka and Claudia Lopez for assistance with data collection, Martin Siegrist, Georg Schmid, Bernard Rutten, Doris Zulauf, Stephanie Kueng (Roche Non-Clinical Biorepository) and Ralf Thoma for technical assistance for biomass and cell line generation. We also acknowledge Nigel Moriarty (Lawrence Berkeley National Laboratories) for help with generation of parameters for DAMGO and general advice for refinement of our model. The work is supported by NIH grant R37DA036246 (B.K.K, S.G. and G.S.) and NIH grant R01GM083118 (B.K.K.). Research reported in this publication was supported by the National Institute of General Medical Sciences of the National Institutes of Health under award number T32GM007276 (A.K.). The content is solely the responsibility of the authors and does not necessarily represent the official view of the National Institutes of Health. Shoji Maeda was supported by the Roche Postdoctoral Fellowship (RPF ID: 113). Gebhard F.X. Schertler acknowledges the Swiss National Science Foundation for grants 310030_153145 and 310030B_17335 (to G.F.X.S.) and long-term financial support from the Paul Scherrer Institute. Brian Kobilka is a Chan-Zuckerberg Biohub Investigator.

References

1. Matthes HW, et al. Loss of morphine-induced analgesia, reward effect and withdrawal symptoms in mice lacking the mu-opioid-receptor gene. Nature. 383:819–823.1996; [PubMed: 8893006]
2. Barnett ML, Olenski AR, Jena AB. Opioid-Prescribing Patterns of Emergency Physicians and Risk of Long-Term Use. N Engl J Med. 376:663–673.2017; [PubMed: 28199807]
3. Connor M, Christie MD. Opioid receptor signalling mechanisms. Clin Exp Pharmacol Physiol. 26:493–499.1999; [PubMed: 10405772]
4. Raffa RB, Martinez RP, Connelly CD. G-protein antisense oligodeoxyribonucleotides and mu-opioid supraspinal antinociception. Eur J Pharmacol. 258:R5–7.1994; [PubMed: 7925586]
5. Raehal KM, Walker JKL, Bohn LM. Morphine side effects in beta-arrestin 2 knockout mice. J Pharmacol Exp Ther. 314:1195–1201.2005; [PubMed: 15917400]
6. Schmid CL, et al. Bias Factor and Therapeutic Window Correlate to Predict Safer Opioid Analgesics. Cell. 171:1165–1175.e13.2017; [PubMed: 29149605]
7. DeWire SM, et al. A G protein-biased ligand at the μ-opioid receptor is potently analgesic with reduced gastrointestinal and respiratory dysfunction compared with morphine. J Pharmacol Exp Ther. 344:708–717.2013; [PubMed: 23300227]
8. Manglik A, et al. Structure-based discovery of opioid analgesics with reduced side effects. Nature. 537:185–190.2016; [PubMed: 27533032]
9. Rasmussen SGF, et al. Crystal structure of the β2 adrenergic receptor-Gs protein complex. Nature. 477:549–555.2011; [PubMed: 21772288]
10. Zhang Y, et al. Cryo-EM structure of the activated GLP-1 receptor in complex with a G protein. Nature. 546:248–253.2017; [PubMed: 28538729]

11. Liang YL, et al. Phase-plate cryo-EM structure of a class B GPCR-G-protein complex. Nature. 546:118–123.2017; [PubMed: 28437792]
12. Huang W, et al. Structural insights into μ-opioid receptor activation. Nature. 524:315–321.2015; [PubMed: 26245379]
13. Ballesteros, JA, Weinstein, H. Receptor Molecular Biology. Vol. 25. Elsevier; 1995. 366–428.
14. Manglik A, et al. Crystal structure of the μ-opioid receptor bound to a morphinan antagonist. Nature. 485:321–326.2012; [PubMed: 22437502]
15. Granier S, et al. Structure of the delta opioid receptor bound to naltrindole. 2012; doi: 10.2210/pdb4ej4/pdb
16. Wu H, et al. Structure of the human κ-opioid receptor in complex with JDTic. Nature. 485:327–332.2012; [PubMed: 22437504]
17. Che T, et al. Structure of the Nanobody-Stabilized Active State of the Kappa Opioid Receptor. Cell. 172:55–67.e15.2018; [PubMed: 29307491]
18. Fenalti G, et al. Structural basis for bifunctional peptide recognition at human δ-opioid receptor. Nat Struct Mol Biol. 22:265–268.2015; [PubMed: 25686086]
19. Emmerson PJ, Liu MR, Woods JH, Medzihradsky F. Binding affinity and selectivity of opioids at mu, delta and kappa receptors in monkey brain membranes. J Pharmacol Exp Ther. 271:1630–1637.1994; [PubMed: 7996478]
20. Minami M, et al. DAMGO, a mu-opioid receptor selective ligand, distinguishes between mu-and kappa-opioid receptors at a different region from that for the distinction between mu- and delta-opioid receptors. FEBS Lett. 364:23–27.1995; [PubMed: 7750536]
21. DiMaio J, Schiller PW. A cyclic enkephalin analog with high in vitro opiate activity. Proc Natl Acad Sci USA. 77:7162–7166.1980; [PubMed: 6261242]
22. Rasmussen SGF, et al. Structure of a nanobody-stabilized active state of the β(2) adrenoceptor. Nature. 469:175–180.2011; [PubMed: 21228869]
23. Wall MA, et al. The structure of the G protein heterotrimer Gi alpha 1 beta 1 gamma 2. Cell. 83:1047–1058.1995; [PubMed: 8521505]
24. Dror RO, et al. SIGNAL TRANSDUCTION. Structural basis for nucleotide exchange in heterotrimeric G proteins. Science. 348:1361–1365.2015; [PubMed: 26089515]
25. Van Eps N, et al. Interaction of a G protein with an activated receptor opens the interdomain interface in the alpha subunit. Proceedings of the National Academy of Sciences. 108:9420–9424.2011;
26. Kaya AI, et al. A conserved phenylalanine as a relay between the α5 helix and the GDP binding region of heterotrimeric Gi protein α subunit. J Biol Chem. 289:24475–24487.2014; [PubMed: 25037222]
27. Chung KY, et al. Conformational changes in the G protein Gs induced by the β2 adrenergic receptor. Nature. 477:611–615.2011; [PubMed: 21956331]
28. Choe HW, et al. Crystal structure of Metarhodopsin II in complex with a C-terminal peptide derived from the Galpha subunit of transducin. 2011; doi: 10.2210/pdb3pqr/pdb
29. Conklin BR, Farfel Z, Lustig KD, Julius D, Bourne HR. Substitution of three amino acids switches receptor specificity of Gq alpha to that of Gi alpha. Nature. 363:274–276.1993; [PubMed: 8387644]
30. Isberg V, et al. Generic GPCR residue numbers - aligning topology maps while minding the gaps. Trends Pharmacol Sci. 36:22–31.2015; [PubMed: 25541108]
31. Isberg V, et al. GPCRDB: an information system for G protein-coupled receptors. Nucleic Acids Res. 42:D422–5.2014; [PubMed: 24304901]
32. Ravindranathan A, et al. Functional characterization of human variants of the mu-opioid receptor gene. Proceedings of the National Academy of Sciences. 106:10811–10816.2009;
33. Skorpen F, et al. The rare Arg181Cys mutation in the μ opioid receptor can abolish opioid responses. Acta Anaesthesiol Scand. 60:1084–1091.2016; [PubMed: 27113810]
34. Chaipatikul V, Loh HH, Law PY. Ligand-selective activation of mu-oid receptor: demonstrated with deletion and single amino acid mutations of third intracellular loop domain. J Pharmacol Exp Ther. 305:909–918.2003; [PubMed: 12626655]

35. West RE, Moss J, Vaughan M, Liu T, Liu TY. Pertussis toxin-catalyzed ADP-ribosylation of transducin. Cysteine 347 is the ADP-ribose acceptor site. J Biol Chem. 260:14428–14430.1985; [PubMed: 3863818]
36. Okude J, et al. Identification of a Conformational Equilibrium That Determines the Efficacy and Functional Selectivity of the μ-Opioid Receptor. Angew Chem Int Ed Engl. 54:15771–15776.2015; [PubMed: 26568421]
37. Gregorio GG, et al. Single-molecule analysis of ligand efficacy in β2AR-G-protein activation. Nature. 547:68–73.2017; [PubMed: 28607487]
38. Qin K, Dong C, Wu G, Lambert NA. Inactive-state preassembly of G(q)-coupled receptors and G(q) heterotrimers. Nat Chem Biol. 7:740–747.2011; [PubMed: 21873996]
39. Maeda S, et al. Crystallization Scale Preparation of a Stable GPCR Signaling Complex between Constitutively Active Rhodopsin and G-Protein. PLoS ONE. 9:e98714.2014; [PubMed: 24979345]
40. Westfield GH, et al. Structural flexibility of the G alpha s alpha-helical domain in the beta2-adrenoceptor Gs complex. Proceedings of the National Academy of Sciences. 108:16086–16091.2011;
41. Zheng S, Palovcak E, Armache JP, Cheng Y, Agard D. Anisotropic Correction of Beam-induced Motion for Improved Single-particle Electron Cryo-microscopy. 2016; doi: 10.1101/061960
42. Zhang K. Gctf: Real-time CTF determination and correction. Journal of Structural Biology. 193:1–12.2016; [PubMed: 26592709]
43. Scheres SHW. Journal of Structural Biology. Journal of Structural Biology. 180:519–530.2012; [PubMed: 23000701]
44. Grigorieff N. FREALIGN: high-resolution refinement of single particle structures. Journal of Structural Biology. 157:117–125.2007; [PubMed: 16828314]
45. Penczek PA, Grassucci RA, Frank J. The ribosome at improved resolution: new techniques for merging and orientation refinement in 3D cryo-electron microscopy of biological particles. Ultramicroscopy. 53:251–270.1994; [PubMed: 8160308]
46. Grigorieff N. Frealign: An Exploratory Tool for Single-Particle Cryo-EM. Meth Enzymol. 579:191–226.2016; [PubMed: 27572728]
47. Adams PD, et al. The Phenix software for automated determination of macromolecular structures. Methods. 55:94–106.2011; [PubMed: 21821126]
48. Heymann JB, Belnap DM. Bsoft: image processing and molecular modeling for electron microscopy. Journal of Structural Biology. 157:3–18.2007; [PubMed: 17011211]
49. Emsley P, Cowtan K. Coot: model-building tools for molecular graphics. Acta Crystallogr D Biol Crystallogr. 60:2126–2132.2004; [PubMed: 15572765]
50. Wang RYR, et al. Automated structure refinement of macromolecular assemblies from cryo-EM maps using Rosetta. eLife. 5:352.2016;
51. Williams CJ, et al. MolProbity: More and better reference data for improved all-atom structure validation. Protein Sci. 27:293–315.2018; [PubMed: 29067766]
52. Schüttelkopf AW, van Aalten DMF. PRODRG: a tool for high-throughput crystallography of protein-ligand complexes. Acta Crystallogr D Biol Crystallogr. 60:1355–1363.2004; [PubMed: 15272157]
53. Friesner RA, et al. Glide: a new approach for rapid, accurate docking and scoring. 1 Method and assessment of docking accuracy. J Med Chem. 47:1739–1749.2004; [PubMed: 15027865]
54. Lomize MA, Lomize AL, Pogozheva ID, Mosberg HI. OPM: orientations of proteins in membranes database. Bioinformatics. 22:623–625.2006; [PubMed: 16397007]
55. Betz R. Dabble. 2017; doi: 10.5281/zenodo.836914
56. Best RB, Mittal J, Feig M, MacKerell AD. Inclusion of many-body effects in the additive CHARMM protein CMAP potential results in enhanced cooperativity of α-helix and β-hairpin formation. Biophys J. 103:1045–1051.2012; [PubMed: 23009854]
57. Best RB, et al. Optimization of the additive CHARMM all-atom protein force field targeting improved sampling of the backbone φ, ψ and side-chain χ(1) and χ(2) dihedral angles. J Chem Theory Comput. 8:3257–3273.2012; [PubMed: 23341755]

58. Huang J, MacKerell AD. CHARMM36 all-atom additive protein force field: validation based on comparison to NMR data. J Comput Chem. 34:2135–2145.2013; [PubMed: 23832629]

59. Klauda JB, et al. Update of the CHARMM all-atom additive force field for lipids: validation on six lipid types. J Phys Chem B. 114:7830–7843.2010; [PubMed: 20496934]

60. Huang J, et al. CHARMM36m: an improved force field for folded and intrinsically disordered proteins. Nat Meth. 14:71–73.2016;

61. Salomon-Ferrer R, Götz AW, Poole D, Le Grand S, Walker RC. Routine Microsecond Molecular Dynamics Simulations with AMBER on GPUs. 2 Explicit Solvent Particle Mesh Ewald. J Chem Theory Comput. 9:3878–3888.2013; [PubMed: 26592383]

62. Case DA, et al. Amber 2017.

63. Hopkins CW, Le Grand S, Walker RC, Roitberg AE. Long-Time-Step Molecular Dynamics through Hydrogen Mass Repartitioning. J Chem Theory Comput. 11:1864–1874.2015; [PubMed: 26574392]

64. Roe DR, Cheatham TE III. PTRAJ and CPPTRAJ: Software for Processing and Analysis of Molecular Dynamics Trajectory Data. J Chem Theory Comput. 9:3084–3095.2013; [PubMed: 26583988]

65. Humphrey W, Dalke A, Schulten K. VMD: Visual molecular dynamics. Journal of Molecular Graphics. 14:33–38.1996; [PubMed: 8744570]

66. Nguyen CN, Young TK, Gilson MK. Grid inhomogeneous solvation theory: hydration structure and thermodynamics of the miniature receptor cucurbit[7]uril. J Chem Phys. 137:044101.2012; [PubMed: 22852591]

67. Nguyen C, Gilson MK, Young T. Structure and Thermodynamics of Molecular Hydration via Grid Inhomogeneous Solvation Theory. arXiv.org. 2011

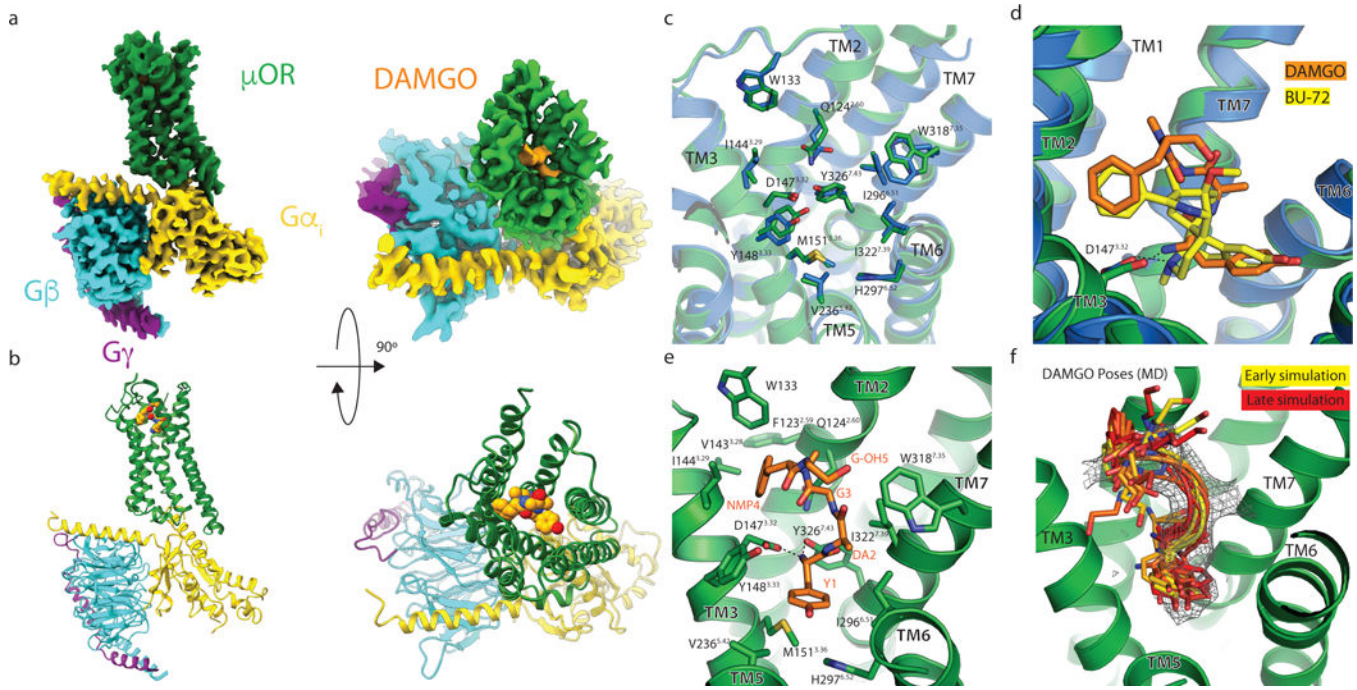

Figure 1. Cryo-EM structure of the μOR-G_i complex

a, Orthogonal views of the cryo-EM density map of the μOR-G_i heterotrimer complex colored by subunit (μOR in green, DAMGO in orange, $G\alpha_s$ Ras-like domain in gold, Gβ in cyan, Gγ in purple). **b**, Model of the μOR-G_i complex in the same views and color scheme as shown in **a**. **c**, Residues that line the μOR orthosteric binding pocket are shown as sticks for the μOR-G_i complex (green) and the μOR-Nb39 complex (PDB 5C1M; blue). The binding pocket residues of DAMGO and BU-72 occupied μOR show nearly identical conformations, despite differences in ligand structure. **d**, Comparison of BU-72 (yellow carbons) in the orthosteric pocket of the μOR-Nb39 complex (blue) with DAMGO (orange carbons) in the orthosteric pocket of the μOR-G_i complex (green). **e**, view of DAMGO in the orthosteric binding pocket with critical residues shown. **f**, A frame from every 100 ns of a 1 μs MD simulation (yellow for t = 0 fading to red for t = 1 μs) shows that the first 4 residues of DAMGO (bottom) are stable, whereas the C-terminal Gly-ol (top) is dynamic but frequently returns to the modeled pose.

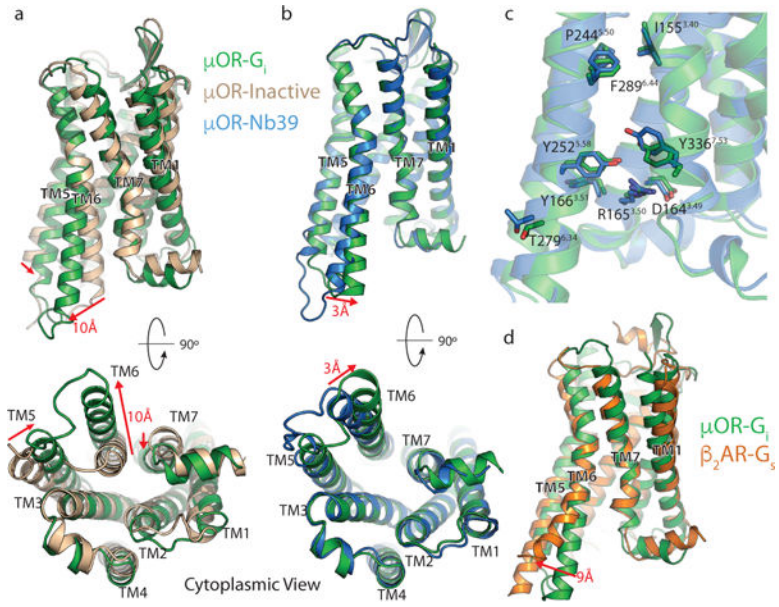

Figure 2. Structural changes in the μOR stabilized by nucleotide-free G_i

a, Comparison of inactive μOR (brown) and the G_i stabilized active state of μOR (green). **b**, Comparison of Nb39 and G_i stabilized active states of the μOR (blue and green, respectively). The structures are nearly identical except for a slight shift of TM6 towards TM7 in the G_i -bound state. **c**, Residues important for activation of the μOR show nearly identical conformations despite the difference in ligands. **d**, Comparison of G_s-stabilized β_2AR (orange) and G_i-stabilized μOR (green). While most transmembrane helices align well between the two receptors, TM6 is kinked further outward by 9Å in the β_2AR. Distance calculated between Cα of residue 6.29 (Ballesteros-Weinstein numbering) in TM6.

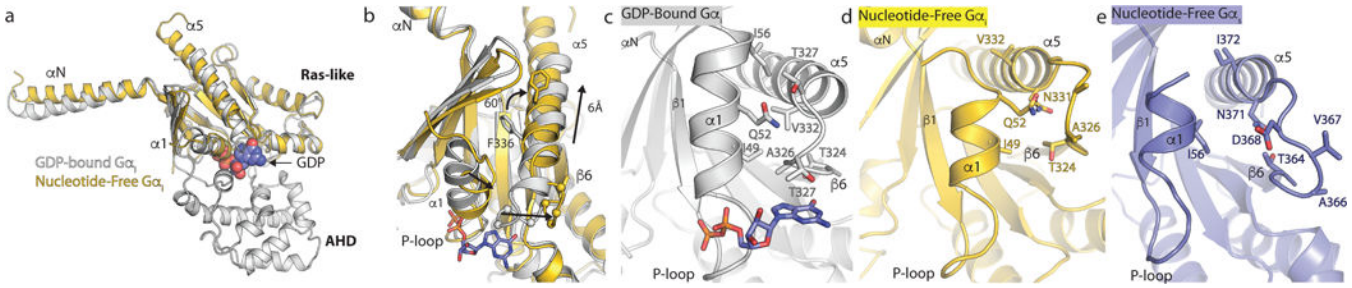

Figure 3. Changes in Gi upon coupling to the μOR

a, **b**, Comparison of GDP-bound $G\alpha_i$ (PDB 1GP2, grey) and nucleotide-free $G\alpha_i$ from the μOR-G_i complex (gold). GDP is shown as blue spheres in panel **a** and sticks in panel **b**. The primary differences between these two structures are the opening and outward movement of the alpha helical domain (AHD), and an upward shift of the α5 helix by 6Å to engage the receptor core. The α-carbons of the TCAT motif are represented as spheres in panel **b**. The TCAT motif coordinates the guanosine base of GDP. The upward shift of the α5 helix and repositioning of the TCAT motif leads to nucleotide release. **c**, **d**, **e**, The interface between the α1 helix and the N-terminal end of the α5 helix and TCAT motif for GDP-bound $G\alpha_i$ (**c**), nucleotide free $G\alpha_i$ (**d**), and nucleotide free G_s from the β_2AR -G_s complex (**e**). The upward movement of the α5 helix disrupts the interaction between the α1 and α5 helices leading to changes in the P-loop that coordinates the phosphates of GDP.

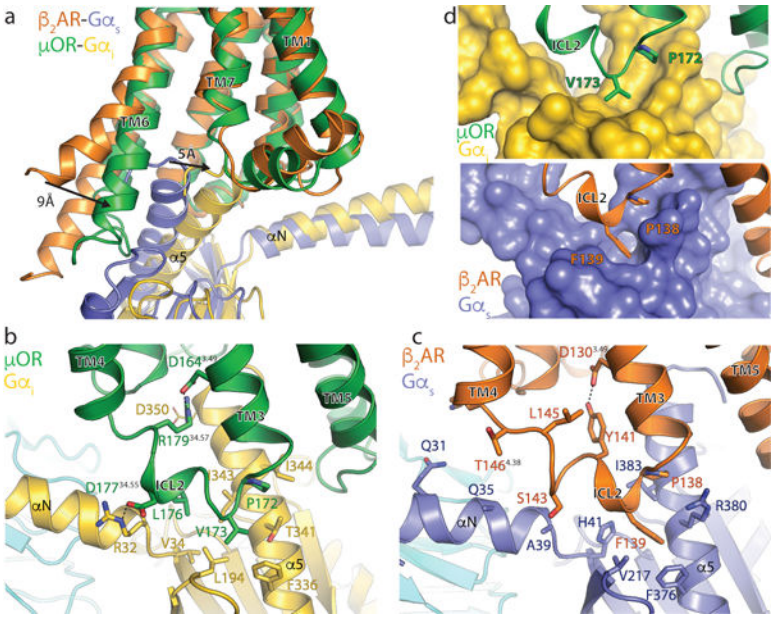

Figure 4. Comparison of the receptor-G protein binding interfaces of the μOR-Gi and β_2AR-Gs complexes

a, Comparison of the conformation of the α5 helix of Gα and receptor TM6 in β_2AR-G_s and μOR-G_i complexes after alignment on the receptor. **b**, Interactions between ICL2 of the μOR (green) and $G\alpha_i$ (gold). Asp 350 of $G\alpha_i$ is depicted with narrow lines to indicate uncertainty in its conformation due to poor cryo-EM density for its side chain. **c**, Interactions between ICL2 of the β_2AR (orange) and $G\alpha_s$ (blue). **d**, Surface view of the hydrophobic pockets in $G\alpha_i$ (top panel) and $G\alpha_s$ (bottom panel) that interact with a non-polar amino acid in ICL2 of the μOR and β_2AR, respectively.

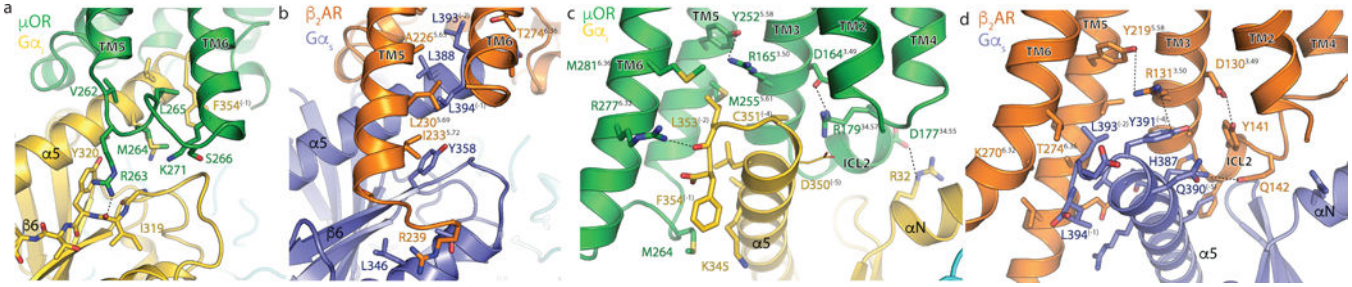

Figure 5. Comparison of the receptor-G protein binding interfaces of the μOR-Gi and β_2AR-Gs complexes

Top panels show interactions between ICL3 of μOR and $G\alpha_i$ (**a**) and between the cytosolic ends of TMs 3,5,6, of the μOR and the α5 helix of G_i (**b**). Asp 350 of $G\alpha_i$ is depicted with narrow lines to indicate uncertainty in its position due to poor cryo-EM density for its side chain. Bottom panels show these same interfaces between β_2AR and G_s (**c,d**).